CONCENTRATION FIELD OF PASSIVE SCALAR IN A MULTI-PHASE PLUME: EXPERIMENTAL STUDY ON APPLYING OF THE 3D-PLIF TECHNIQUE AND ITS APPLICATION FOR DESIGN OF SUBSEA INJECTION SYSTEM OF DISPERSANT

A Dissertation

by

VADOUD DEHKHARGHANIAN

Submitted to the Office of Graduate and Professional Studies of
Texas A&M University
in partial fulfillment of the requirements for the degree of

DOCTOR OF PHILOSOPHY

Chair of Committee,	Scott A. Socolofsky
Committee Members,	Kuang-An Chang
	Robert Hetland
	Yassin A. Hassan
Head of Department,	Robin Autenrieth

December 2016

Major Subject: Civil Engineering

ABSTRACT

In this research, we used experiments to measure the passive concentration field inside a multi-phase plume with an application to help design an injection system for subsea injection of dispersant during an accidental blowout. 3D Planar Laser Induced Fluorescence (3D-PLIF) technique was adapted to study the spatial distribution of the concentration field created by different types of injectors. This technique requires new correction processes to account for the presence effects of the immiscible particles in the field of view. We used the developed method to measure the concentration field inside a bubble plume with different flow rates to investigate the effects of different injectors on the characteristics of the passive scalar concentration field.

We derived new correction processes to convert fluorescent light intensity to concentration, such as an image processing method to detect and remove the signature of bubbles and shadows from an image and an object detection method to specifically find bubbles and calculate the presence probability inside the bubble plume. Based on the bubble concentration, the laser attenuation can be estimated, which is required for accurate concentration measurements.

We used our developed 3D-PLIF technique to measure the concentration field created by three types of injector: single point, wand, and collar diffusor to study the effects of injection geometry as well as injection position on the characteristics of the concentration field.

To my family:

Baba Mohammad

Maman Roya

Samin joon

ACKNOWLEDGEMENTS

I sincerely express my gratitude to my advisor, Dr. Scott A. Socolofsky, for his indispensable guidance extended to me through my entire degree program. He was a true example of dedicated teacher and mentor for me while I was working with him. Without his dedication and support, it was not possible for me to finish this project. I deeply appreciate his leadership and managing effort he put to inspire us to achieve our goals.

I also would like to extend my gratefulness to my committee members, Dr. Kuang-An Chang, Dr. Robert Hetland, and Dr. Yassin A. Hassan for their kind words of wisdom and instruction to make improve the outcome of this research. I am also thankful to Mr. John Reed for his advice and help during my experimenting part of my work.

Besides my studies, I am beholden to all my friends for their support and encouragement and for their unsparing help and advice.

Last but not least, I strongly believe that without sacrifice and support of my beloved family I could not be here at this point of my life.

This research was funded through the Chevron-MITEI University Partnership Program. This support is gratefully acknowledged.

TABLE OF CONTENTS

Page

LIST OF FIGURES

Page

LIST OF TABLES

Page

1 INTRODUCTION

1.1 Problem statement

Multi-phase plumes have been studied extensively during past years to investigate their different properties. For this purpose, laboratory methods have been used to elucidate the plume behavior under different conditions such as unstratified ambient (Rooney and Linden 1996), stratified ambient (Ferrier et al. 1993, McGinnis et al. 2004, Socolofsky and Adams 2005), and in the presence of cross flow (Socolofsky and Adams 2002) . Additionally, field studies have investigated the effect of multi-phase plumes on their ambient environment in real world applications (McGinnis, Lorke, Wüest, Stöckli and Little 2004, Schladow 1992). In the numerical field, various models have been developed (Bombardelli et al. 2007, Buscaglia et al. 2002, Socolofsky and Bhaumik 2008, Wüest et al. 1992) to investigate the flow characteristics of multi-phase plumes. In all of these research activities, the bulk parameters of the plume such as mean velocity profile (Milgram 1983, Seol et al. 2007), volume flux (Leitch and Baines 1989), and mean concentration and temperature profiles (Papantoniou and List 1989) were the area of interest. This dissertation aims to measure the mean and turbulent structure of the passive scalar concentration field inside a multi-phase plume in a quiescent an, unstratified ambient. This situation is of interests because it is similar in nature to subsea dispersant injection during an accidental oil well blowout.

1.2 Objectives of study

We want to measure the resulted instantaneous concentration field of a passive scalar inside a multi-phase plume from different tracer injection designs. For this purpose, we conducted our experimental studies considering three different injection tools. The created concentration

fields of a passive scalar were recorded using a non-intrusive 3D Laser Induced Fluorescence (3DLIF) technique. To obtain correct data, we developed additional correction processes in order to consider the presence of immiscible particles in the dataset. These processes include the detection and removal of immiscible particles from the image dataset using the intensity threshold values. The reason for removing the footprints of immiscible particles is that their intensity origin is different from the passive scalar's intensity source. The other correction process is addressing the local intensification effect of bubbles on the amount of lighting in their vicinity resulting from reflections at the bubble-water interface. To remove this effect, the amount of intensity build-up was correlated to the probability of the presence of bubbles in the plume and then this value was calculated using a novel object detection process for bubbles specifically.

The duration time of our experiments was long enough to ensure that more than one plume-wandering period was recorded. This resulted in a large dataset that required our correction processes to be autonomous for analysis. This goal was achieved by using machine learning algorithms. The developed concentration field measurement technique enables us study the efficiency of different injection systems, which helps to design the most efficient injection system in the case of future subsea blow out accidents.

1.3 Applications of the study

By completing this research, we will develop a concentration field measurement technique that has applications in other fields of study and industrial activities. The first application of this method is to design an efficient injection system for the subsea injection of dispersant. In the DeepWater Horizon accident, the dispersant was injected into the source of the blow out

for the first time in a large-scale quantity. Kujawinski et al. (2011) studied the fate of injected dispersant, COREXIT 9500, during the flow of expelled oil and gas and after the flow had stopped by tracing one of the components of COREXIT 9500, the anionic surfactant DOSS. They concluded that the detailed analysis of the mixing process of the dispersant inside the released plume is necessary to resolve the efficiency of a subsea dispersant application method. Our developed measurement technique makes this analysis possible to better understand the fate of the oil and injected dispersant.

One of the simultaneous processes of turbulent plumes is the entraining of the ambient fluid into the rising plume, which consequently mixes the ambient environment. In the case of a subsea oil well blowout, passive sea creatures along with seawater are entrained into the plume and exposed to the toxic components of the rising hydrocarbon plume. Resolving the concentration field of passive scalar inside multi-phase plumes, thus, expands the knowledge of environmental impacts of the blowout accident.

Another application for this study could be in industrial implementations of multi-phase plumes. The mixing ability of multi-phase plumes is often used inside boilers, chemical reactors, and nuclear reactors. Resolving the concentration field inside these facilities results in improving the quality of the final product as well as more efficient processes. Applying our developed method can assure the achievement of this goal.

1.4 Dissertation organization

This dissertation is organized as follows. The second section presents the developed image processing technique to account for the presence of immiscible particles in our image dataset and applying the required corrections to convert light intensity to concentration. In section

three we present the measurement results from one of our test cases and demonstrate the correctness of our method by comparing the calculated concentration values with the measured values during the experiments. Analyzed data from all of our experiments and evaluating of the efficient injection system for the subsea dispersant application is presented in section four. The last section includes the summary and recommendations for the future work on this subject.

2 IMAGE ANALYSIS METHOD TO REMOVE BUBBLE SIGNATURES FROM PLIF IMAGES IN A BUBBLE PLUME

2.1 Introduction

Image processing intends to improve (Andrews and Hunt 1977, Banham and Katsaggelos 1997, Katsaggelos 2012), decipher (Carmichael et al. 2010, Leutenegger et al. 2011, Rohlfing et al. 2004), and extract data (Dalal and Triggs 2005, Gall et al. 2011, Godec et al. 2013) from a digital image. Developing non-intrusive methods in the field of experimental studies greatly depends on the available imaging systems and associated image processing techniques. The recorded data through the image recoding systems needs to be corrected for possible sources of error, grouped into its constituents, and converted into useful type of information for further analyses. Conducting calibration tests helps to specify the error sources and defines the required corrections as well as extracting the correlations between image intensity to the parameter of interest. Grouping the components of an image requires locating and discriminating of members of the same group from the rest of the image. This process is called object detection. Here, we apply object detection to identify bubbles in a Planar Laser Induced Fluorescence (PLIF) image of a bubble plume and passive tracer. This is required to isolate the tracer information and convert tracer image intensity to concentration.

Object detection techniques try to find the object of interest among many other parts of an image. It can be simply segmenting an image into its components based on one or more threshold values (Gonzalez 2009) or more sophisticated methods that detect an object by its distinct intensity properties comparing to other parts. These are the methods that use the

intensity gradient information to perform the detection task (Gonzalez 2009). When the object of interest has complex intensity properties, techniques using visual features and qualitative properties of the object are appropriate tools to find that object in an image. The advantage of visual features and qualitative properties of an object is that they are invariant to intensity changes, partial exposure, or any other quantitative values comparing to other detection methods. This characteristic makes them suitable for training a machine-learning algorithm (classifier) in order to perform the detection task autonomously.

Machine learning algorithms are useful tools to complete a classification task over a dataset, which consists of different types of information. These algorithms are used when a pattern exists between components of the dataset and this pattern cannot be pinned down mathematically. Also it is important that a large set of data is available in order to extract the existing pattern. In the field of image processing, a classifier can be trained for face detection (Dalal and Triggs 2005), to track an object in a video (Gall, Yao, Razavi, Van Gool and Lempitsky 2011, IBBT 2010), or to categorize different objects in a dataset (Leibe et al. 2008, Yanulevskaya et al. 2014).

In the field of fluid mechanics, measuring properties of different flow structures is an important tool to understand the underlying fluid physics and to verify the accuracy of numerical models developed for predicting those physics. One of the experimental methods for measuring the mixing properties and concentration field of a flow structure is the PLIF technique (Karasso and Mungal 1997, Koochesfahani and Dimotakis 1985). This method uses image-processing analysis to extract the data from the recorded image dataset. Conventional application of the PLIF technique is for measurements of mixing properties of

single-phase flows. Single-phase flows are generated due to the movement of the same state of matter. To expand the application of the PLIF technique to study multi-phase flows (created by displacement of two states of matter in one another), additional correction analyses are necessary to separate the information of each phase. New PLIF corrections to obtain concentration are also needed due to the presence of immiscible particles in the data and the fact that the origin of light intensity values of those particles will be different from the rest of the flow structure.

In this section we want to measure the mixing properties and concentration field inside of a bubble plume by means of the PLIF technique. In order to study the 3D profile of the plume, we expanded the technique into 3DLIF. The recorded images have three major components: visualized flow structure, bubbles, and their associated shadows. The useful part of an image for the PLIF analysis is the visualized flow structure, and we desire to discard the rest of an image. For this reason, these structures (bubbles and shadows) should be detected and removed from the dataset. The detection and removal of the unwanted part of our dataset is the task of image processing analysis. Due to the size of our dataset, which contains more than 50000 images, it is not feasible to perform the analysis manually; hence, we developed a correction method based on the image processing techniques in combination with machine learning algorithms to perform this task autonomously.

2.2 Experimental set-up

Our experiments were carried out in a glass walled tank of 2 m long, 1.5 m wide, and 1.1 m height in the Fluid Dynamics Laboratory in the Zachry Department of Civil Engineering at Texas A&M University. The source of the bubble plume was a cylindrical air stone with 14

mm diameter and 20 mm height. The air stone was placed on the bottom of the tank with equal distance from sidewalls and 0.5 m distance from the front side. The laser source was a 5 Watt continuous wave Nd:Yag laser (532 nm Spectra-Physics Millennia Edge Single Frequency CW). To visualize the flow structure, Rhodamine 6G fluorescent dye was used in these experiments. The laser sheet was made by means of a fast-galvanometer scanning mirror (Model 6220MH60, Cambridge Technology, Inc.) that was mounted on top of a motorized linear stage (A-LST0750B Zaber technologies Inc.) in order to visualize the 3D profile of the bubble plume along a stack of 2D sheets. A Coherent FieldMaxII-TOP power meter measured the laser power fluctuations during experiments. About 10% of laser light power was directed into the power meter by a standard microscope slide (Cowen et al. 2001). A high-resolution CCD camera (Flow Master 3S, 12 bit intensity depth with 1024x1280 pixel resolution) was used to capture the finest details of the flow field using a 35 mm focal length lens. The camera was recording at four frames per second and the exposure time was set to 200 msec. A cut-on optic filter allowing light with wavelength above 543 nm (543AELP, Omega Optical, Inc.) was positioned between the camera lens and the tank to remove reflected laser light (514 nm) while capturing the majority of fluoresced light from the Rhodamine 6G dye (555 nm). The set-up of the experiment is shown in Figure 2-1.

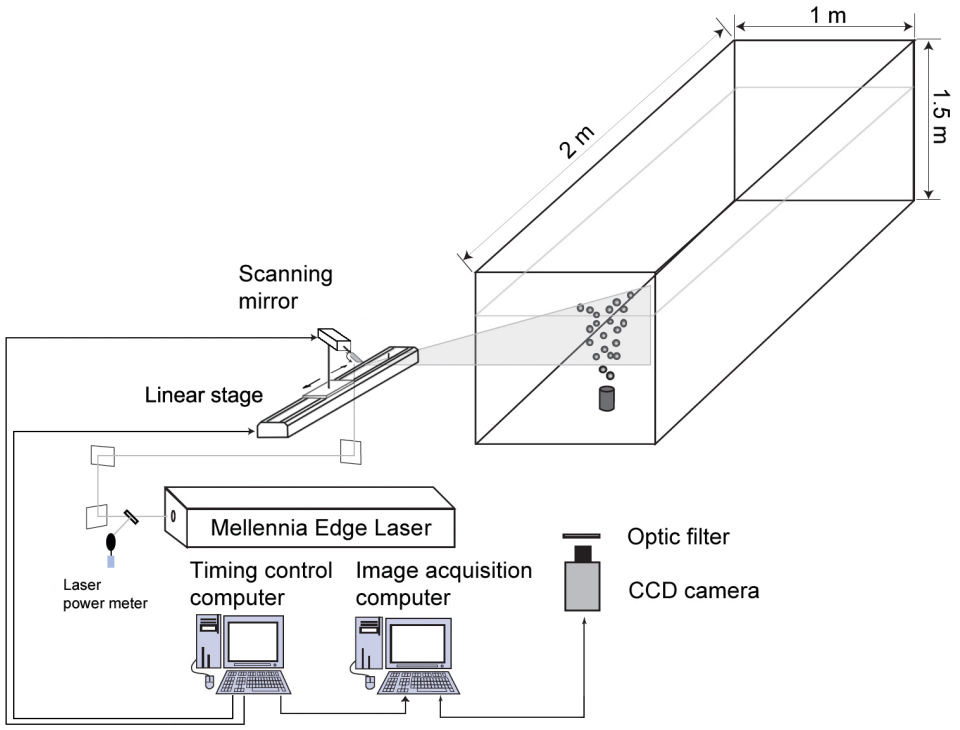

Figure 2-1 Experimental set-up

To develop our correction method, two sets of images were recorded. The first set consisted of images of the plume with a clear background, and the tracer dye was injected into the plume during the course of the experiment. This set of images created our main dataset. Further investigation of the mixing properties and concentration field inside the bubble plume will be performed on this dataset. The second set of images was pictures of the running plume with a uniform premixed dye concentration of a known amount of the tracer dye. We developed our void fraction calculation method and collected a sample pool of bubble instances from this dataset. An example of each type of recorded images is shown in Figure 2-2. The Figure 2-2(a) is the image for dye injection and the Figure 2-2(b) is for a uniform background dye concentration.

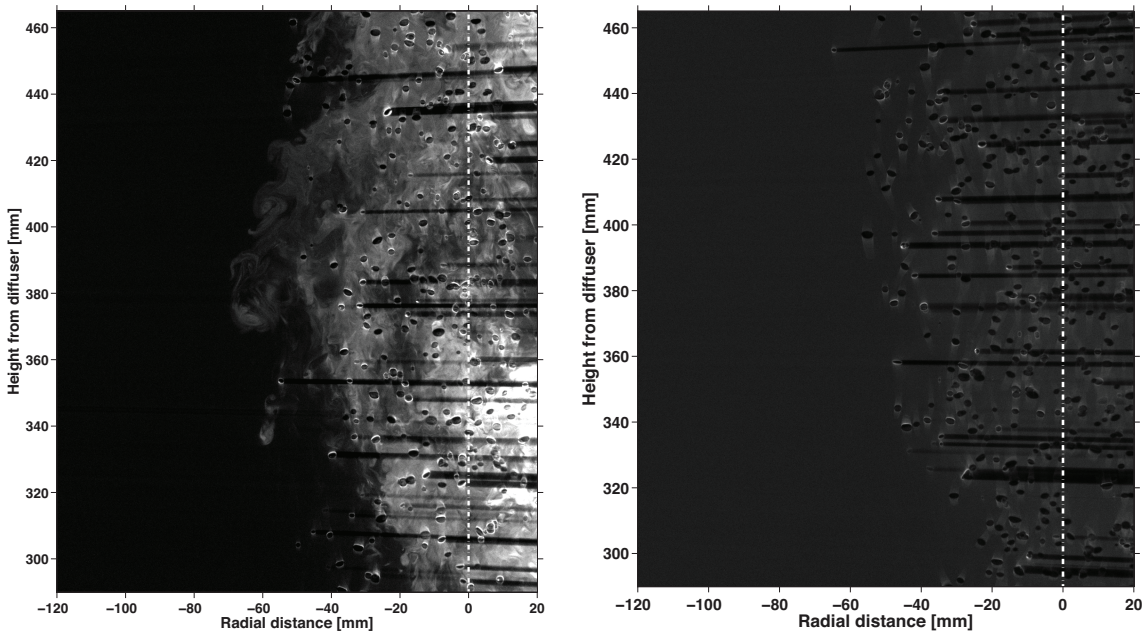

Figure 2-2 Recorded images from experiments

2.3 Correction methods

2.3.1 Symptoms

In the case of conventional PLIF that is measuring the concentration field properties of single-phase flows such as turbulent jets (Feng et al. 2005), waste flow disposal systems (Tian and Roberts 2003), and water disinfection systems (Gandhi et al. 2011), there are developed correction methods such as laser sheet uniformity correction (Crimaldi and Koseff 2001), vignette effect correction (Daviero et al. 2001), corrections for attenuation effects of water and the tracer dye on the laser light power (Ferrier, Funk and Roberts 1993) that have been used for a long time. If we want to implement the PLIF technique to the measurement of multi-phase flows, additional correction steps should be considered to account for the effects of the bubbles. These corrections are mainly due to laser beam reflection and refractive index difference at the bubble-water interface.

The first effect associated with the presence of immiscible particles in the recorded images is their signatures in the dataset. The PLIF technique measures the concentration field and mixing properties based on the correlation of the tracer dye concentration with intensity values in recorded images. If there are any other components in the image that are not due to the tracer dye presence, the PLIF technique is not capable of distinguishing them from the tracer dye. This lack of capability causes false measurement at the position of those components. To solve this problem, the signatures of immiscible particles should be removed. Moreover, if the refraction index of immiscible particles is different than the ambient environment, these particles can block, reflect, and refract the laser beam, creating shadows and overlapping light rays. Just as with the intensity values associated with shadows are not correlated with the amount of tracer dye concentration at their position thus should be removed. Figure 2-3 shows an example of the signature of the immiscible particles and their shadows in our dataset.

The second effect of the presence of immiscible particles in the data set is the laser light reflection from their surface if their refractive index is different from that of the ambient environment. This reflection can happen in any arbitrary direction and if it is aligned with the generated laser sheet, the amount of laser light energy will increase locally in the neighboring area of that particle.

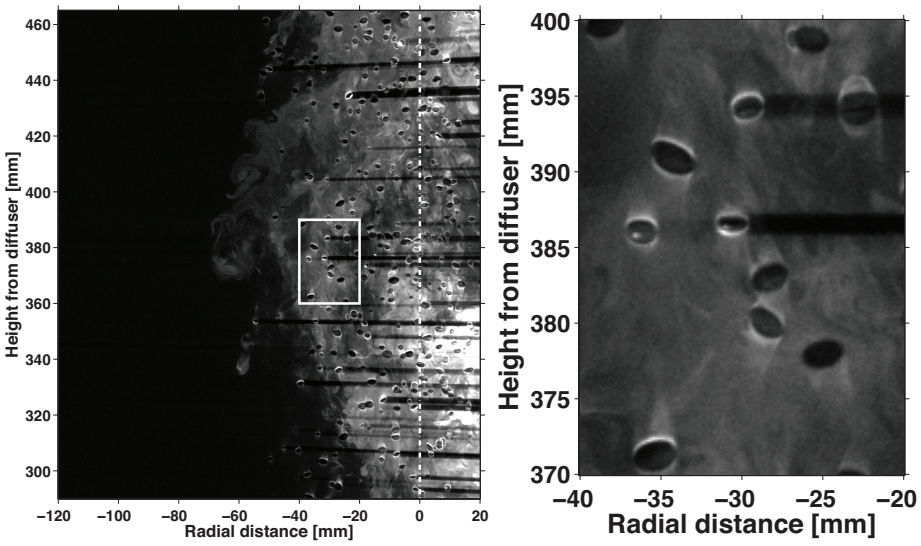

Figure 2-3 Bubble and shadow signatures

Since the PLIF technique cannot distinguish intensity value changes to the change of laser light energy in an image, the calculated results will indicate the higher amount of dye concentration in the affected area, which is not correct. Figure 2-4 shows the time-average light intensity for the case of a uniform background dye concentration. The laser originates from the left-hand-side of the image. As the light passes through the bubble plume, its local intensity increases as reflections and refractions cause the same pixels to be illuminated multiple times during a single sweep of the laser beam through the image. This intensity increases with increasing bubble concentration and must be accounted for to accurately predict the dye concentration from the image intensity.

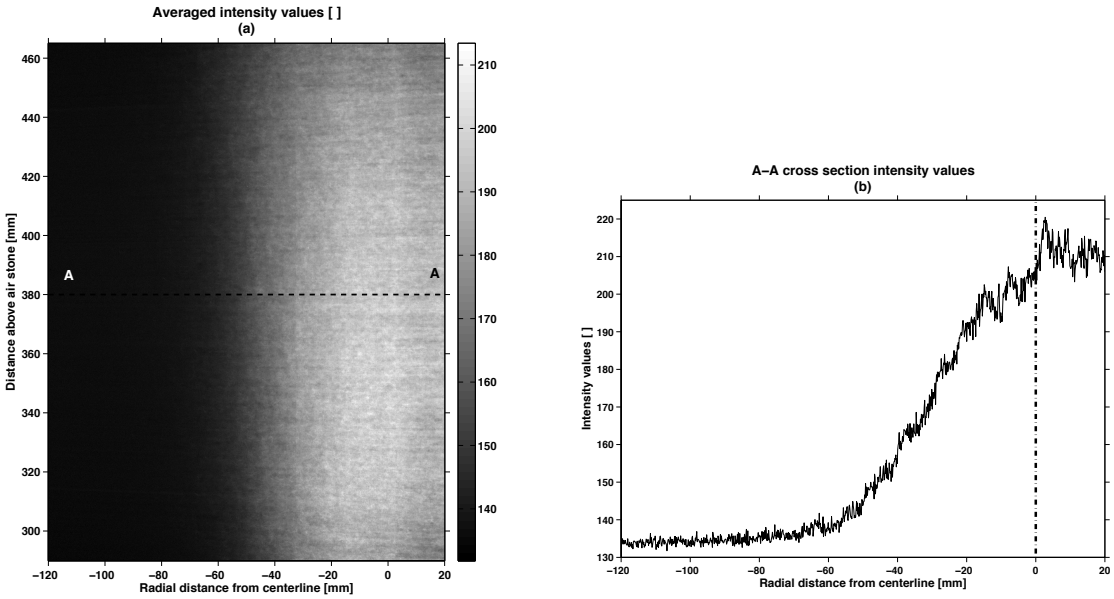

Figure 2-4 Bubbles effect on changing intensity value of laser light

In our experiments, the immiscible particles were air bubbles that have different refractive index from water, so they created all of the above-mentioned errors in our recorded dataset.

2.3.2 Bubble signature removal

The general idea of addressing the first effect of bubble signatures in our image dataset was detecting the bubble instances by the most efficient image processing method and replacing their intensity values with an appropriate flag. There are a variety of detection methods available in the field of image processing, and we used a combination of them to get to the best result possible.

The first stage of the process was detecting bubble instances in our dataset. Because flow structures in the dye have similar size, shape, and intensity to bubbles, finding a bubble solely using the conventional detection methods, such as edge detection or image

segmentation was not possible, but using a combination of these methods was the answer for our problem. In this process, first the border of a bubble is specified by means of an edge detection method. Then the intensity values of centers of bubbles were collected and used to derive the threshold values. In the last stage, the threshold values were used to segment the image into its components and to remove bubbles.

An edge line is a step in the intensity value that can be single-sided, double-sided or sloped (Gonzalez 2009). It can be used to distinguish between homogenous intensity areas beside each other. The edge line information can be extracted by calculating the gradient of the intensity field. There are techniques for edge detection such as first order and second order approaches (Davis 1975), the Canny based edge detection method (Canny 1986), and the most recent technique, the phase congruency based method (Kovesi 1999). The results of applying each of these methods on a sample image of the dataset are shown in Figure 2-5.

It can be seen from Figure 2-5(b) that the first order edge detection method extracts the edge lines in an image with a strong dependency on the strength of the intensity gradient. It is clear from the image that the top and bottom borderline of most of the bubbles are better detected due to their greater intensity gradient compared to the sides of a bubble. The second order approach produced blurred data that was barely usable for the purpose of detection (Figure 2-5(c)). The Canny approach is one of powerful edge detection methods that has limited dependency on the strength of the intensity gradient. This characteristic of the Canny method caused over detection of edge lines in an image. As can be seen Figure 2-5(d), the edge lines of shadows (the horizontal lines) and the tracer dye patches were detected in addition to the border of bubbles.

The last method and the most effective method that we used in our calculation was edge and corner detection based on phase congruency (Kovesi 1999). This method is based on the theory that the edge features of an image is a result of in-phase Fourier components of the image in that position. The advantage of this method compared to other edge detection methods is that it depends on non-dimensional variables of an image that does not change with variation in the intensity values of the image. Figure 2-5(e) shows that the phase congruency method was capable of extracting the edge data of the bubbles as the main results as well as some of the edge lines of the tracer dye patch.

Based on the result of the phase congruency detection method, we wanted to separate the bubble instances from the rest of the edge data map. The common shape of bubble instances in our data is close to an ellipse that guided us to use the shape detection algorithms, in our case ellipses, to find the bubble signatures. One of the easiest and most efficient ways to do this was using the built in function of the image processing toolbox of Matlab. This toolbox has a function named “imfindcircles” that screens an image for possible round objects based on the tuned controlling parameters.

The controlling parameters of the imfindcircles function are: 1) the size range of the round objects. This range in our dataset was correlated to bubble diameters between 5 to 20 pixels based on our observation over the dataset; 2) the roundness sensitivity of the function. After applying the phase congruency technique on our images, the only remaining round objects in the image were bubbles edge lines and based on their shape characteristic, we set the sensitivity of the function to 0.93; and 3) the gradient strength of an object. We completed a

series of calibration tests to define the best value of this parameter for our dataset, with the objective function to maximize the number of correct detection of bubble instances.

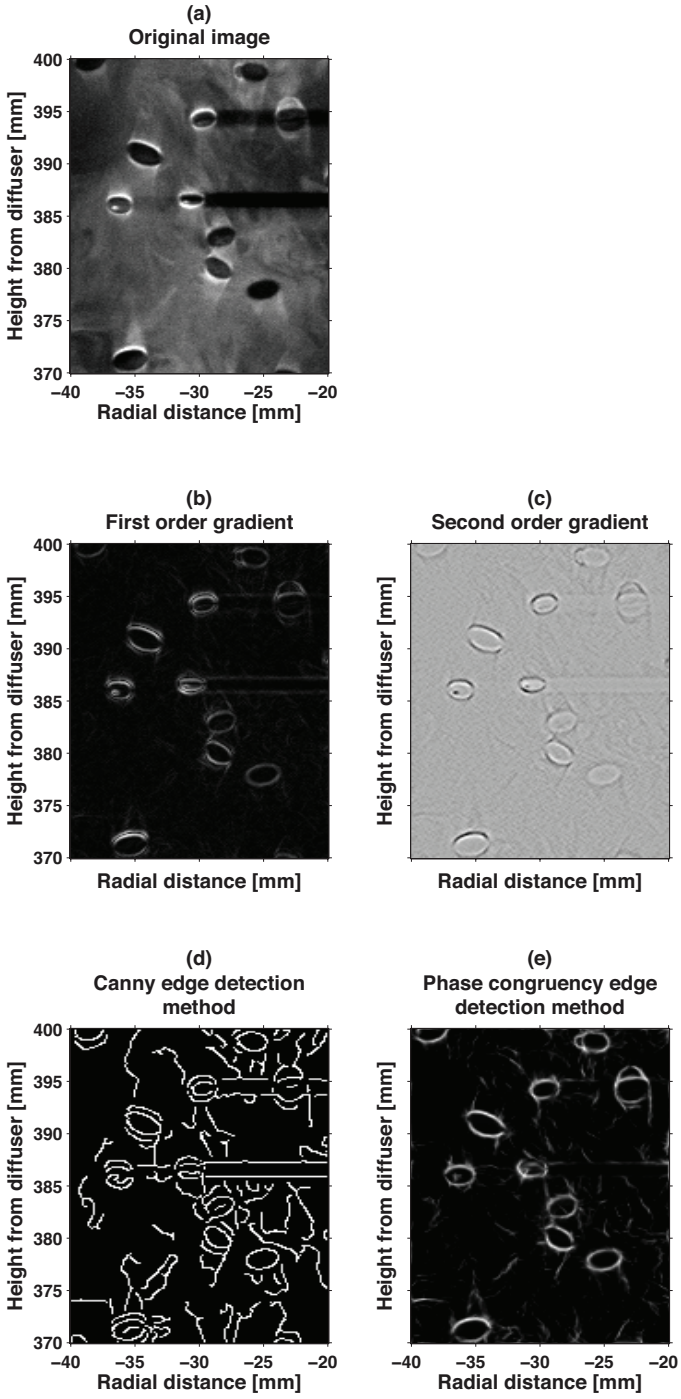

Figure 2-5 Results of different edge detection methods

The result of these tests was the value of 0.3 for the gradient strength.

After finding the position of a bubble, its area on the image should be selected and the intensity values over that area should be replaced with a bubble flag. We used the thresholding method to segment the occupying area by a bubble because the intensity values inside a bubble are comparably smaller than their close vicinity. This characteristic enabled us to detect bubble signatures accurately using sections of an image. Because intensity varied across the image, we selected different threshold values in each of 64 sub-windows of the image. Figure 2-6 shows the interrogation windows for a single image in the dataset.

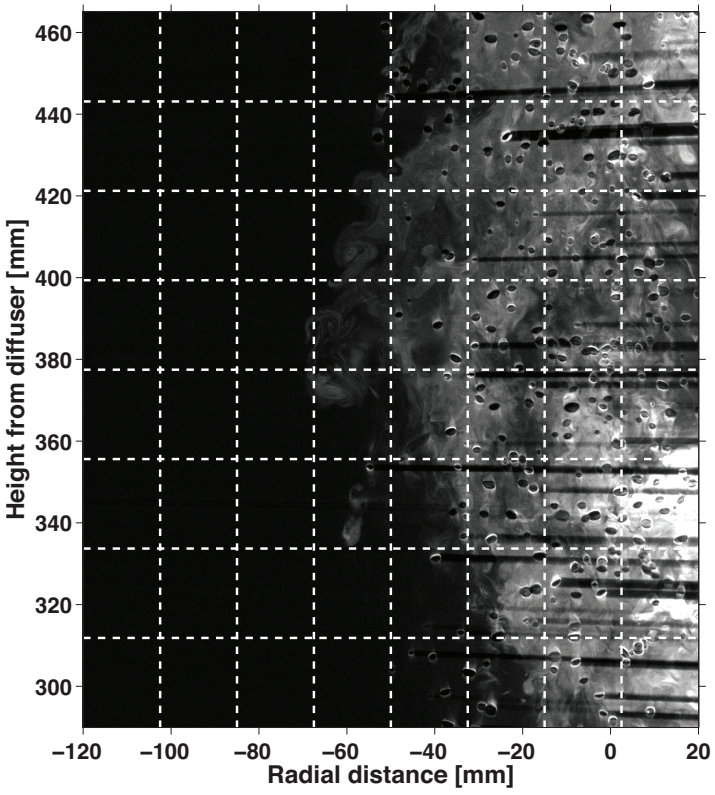

Figure 2-6 Sectioned image

We considered an overlap between sections so that the results of the process for two adjacent sections match together smoothly. The overlap size was chosen based on the diameter of common size of large bubbles in our dataset that was 20 pixels. The padded sub-window with overlap ribbons was first searched to extract its edge information. The result of the edge detection step was then sharpened and smoothed in order to remove the spurious maximals and to clarify the edge line of bubbles. After this step, the imfindcircles function screened the sub-window for possible bubble instances and returned the center position of a bubble and the intensity value on that position. The intensity values were compared with the averaged intensity of the sub-window. Detections with larger intensity values are disregarded due to the intensity properties of bubbles that are smaller comparing to their vicinity.

The centers' intensity values of correct detections were used to calculate the threshold parameters for the segmentation process. For this calculation, the average and standard deviation of center intensities were derived in each sub-window and based on the following formula the threshold values were calculated.

$$i_{k,n} = m_{b,k} \pm 0.5n \cdot \sigma_{b,k}, n = [0,1,2,3,4] \quad (2\text{-}1)$$

Where, $i_{k,n}$ is the threshold value, $m_{b,k}$ is the averaged intensity value of bubble centers in k_{th} sub-window, $\sigma_{b,k}$ is the standard deviation of bubble centers intensity in the same sub-window, and n is the multiplier of the bubble center intensity value standard deviation. In the case of no result from the imfindcircles function, the threshold values of previous sub-window were used for the purpose of thresholding.

Each threshold value $i_{k,n}$, n=[0,1,2,3, and 4] was used to segment the sub-window into two regions: bubbles and non-bubbles, resulting in five segmented position maps. Then, these five position maps were added together and the maximum value of the sum was limited to one to create the final filter map of the bubble positions. Applying this filter to the associated sub-window produced the final results of the bubble removal process. The byproduct of this process was removal of the bubble shadows. This was achieved because shadows have similar intensity properties to bubbles, which both have smaller intensity values comparing to their neighboring pixels.

Finally, reflected light by a bubble creates a local bright region around a bubble that is known as a hot spot. The brightness of these hot spots is a result of excess amount of light energy and not the additional tracer dye concentration. To remove the signature of these hot spots, a smoothing kernel of 15 by 15 pixels was applied to an image and the ratio of the intensity value changed after smoothing to the original intensity values were calculated. Pixels with a ratio of 0.1 and higher were considered as a hot spot point in an image and the intensity value of those pixels were replaced with NaN. The result is shown in Figure 2-7.

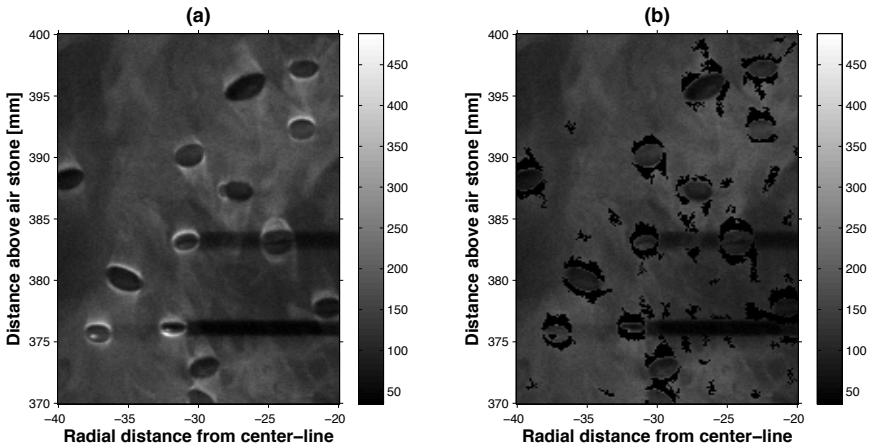

Figure 2-7 Hot spot removal

After all image processing steps are completed, the edited sub-windows were placed back on their position in the whole image after cutting the overlaps. The final result of the correction method for the presence of bubble signatures in our dataset is shown in Figure 2-8.

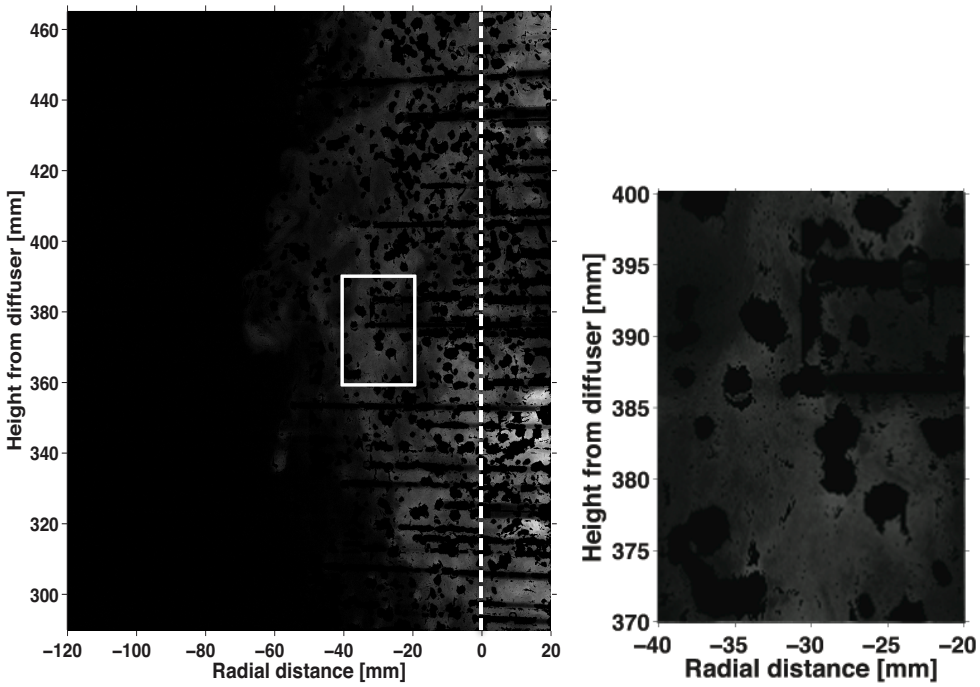

Figure 2-8 Final result of bubble removal method

From this image, it can be seen that a couple of small bubbles and some amount of shadows remained in the image. The associated error with misdetection in our method was calculated as 3% based on manual detection and the number of bubbles in an image for 20 sample images. The flow chart of the bubble removal process is shown in Figure 2-9.

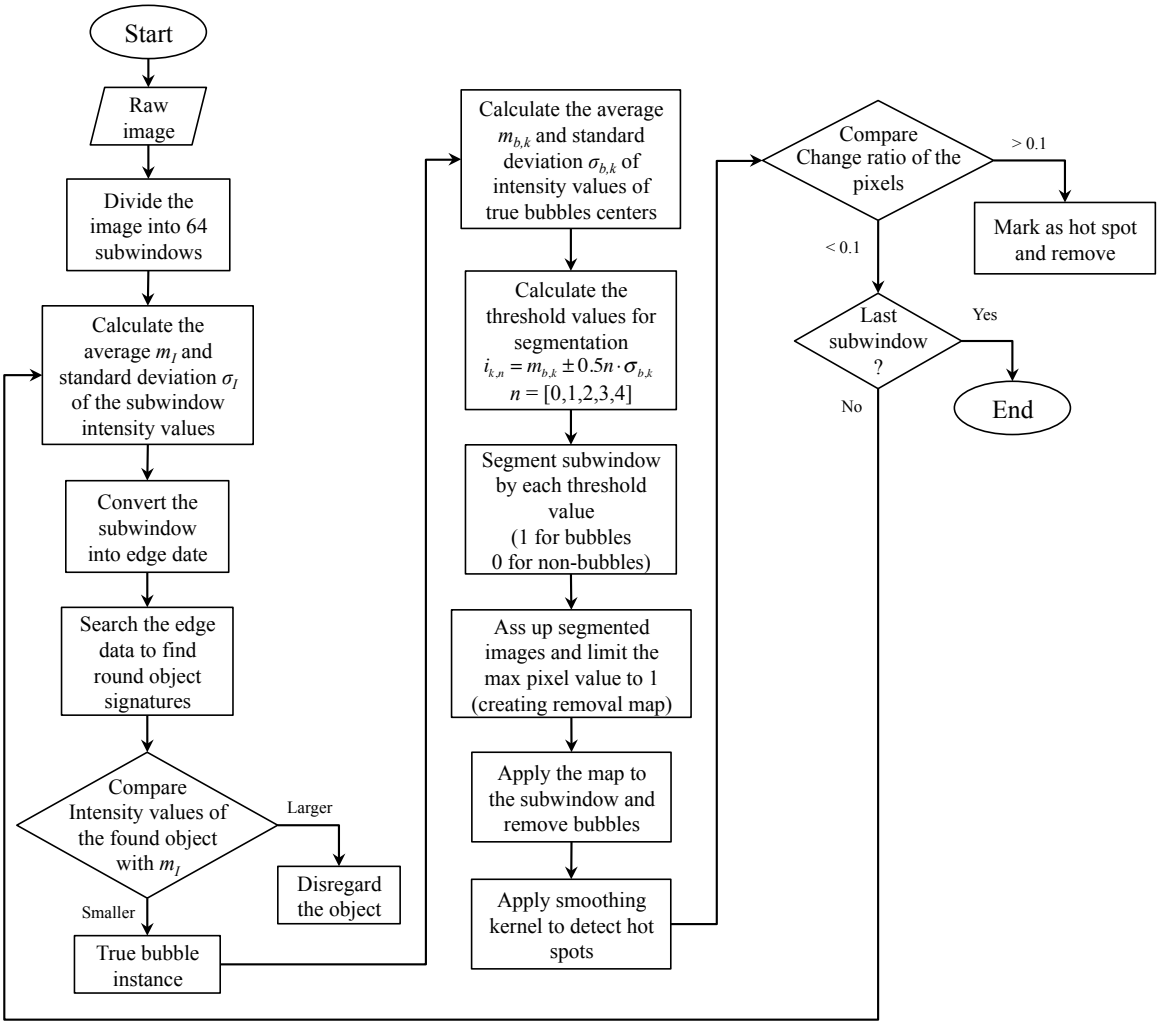

Figure 2-9 Bubble removal flow chart

2.3.3 Correcting laser sheet power variation due to presence of bubbles

The second effect of bubbles' presence on the recorded images from the PLIF technique is the light reflection from the surface of bubbles that disturbs the uniform laser light distribution. The correction method for this effect was first introduced by Seol (2008). He found that the amount of intensification in the laser light energy has a correlation with the void fraction of the bubble plume. A PLIF image of homogenously mixed solution of tracer dye has a uniform intensity value for all of its pixels after applying the standard PLIF corrections. But when bubbles are running in the field of view, the profile of intensity values across the bubble plume shows an increase in the intensity values over the position of the bubble plume. Since there is no change of tracer dye concentration over the field of view, this shift in the intensity values is not a true representation of the concentration field behavior of the bubble plume and needs to be corrected.

Seol (2008) calculated the void fraction of the bubble plume based on the ratio of the amount of presence time of a bubble on each pixel of an image compared to the total time of the experiment.

$$\alpha(i,j) = \frac{\sum_{i,j} t_G(i,j)}{T} \tag{2-2}$$

Where, $t_G(i,j)$ is the amount of time that the bubble presents on pixel (i,j) and T is the total time of the experiment. Knowing the frequency of the recording data can simplify the above formula to:

$$\alpha(i,j) = \frac{\sum_{i,j} n_G(i,j)}{N} \tag{2-3}$$

Where, $n_G(i,j)$ is 0 or 1, zero if there is no bubble and 1 in case of presence of a bubble on the pixel *(i,j)* and *N* is the total number of recorded images. The Seol (2008) image dataset consisted of a limited number of images, and the bubble signatures in his dataset were invariant in size so that he could manually remove the bubbles and calculate the void fraction of his bubble plume. But the number of images and the wide range of bubble sizes in our dataset made it impossible to perform this task manually. For this reason, we used the machine-learning algorithm to detect and count bubbles. We were not able to use our previous method for counting bubbles purpose because our method does not segregate objects based on their nature rather by their intensity values. That is why a bubble or a shadow does not have any difference for our bubble removal method. Here we want to exclusively detect and count bubbles.

The bubble intensification factor was calculated following the same process for calculating of water attenuation factor. The light intensity profile of the image containing bubbles was compared to the light intensity profile of the premixed tank with the uniform dye concentration. Assuming the exponential nature of the intensification, fitting an exponential equation to the light intensity of the image containing bubbles provided us with the bubble intensification factor for our experiments (Eq. (2-4)).

$$I_c\big|_v = \frac{I(r,\theta)}{\exp\left(\int_0^r \alpha(r,\theta)\cdot a_v\, dr\right)} \tag{2-4}$$

Where, $I_c|_v(r,\theta)$ is the corrected intensity value for the light intensification due to bubbles presence, $I(r,\theta)$ is the uncorrected intensity values, $\alpha(r,\theta)$ is the void fraction at point (r,θ), and a_v is the void fraction amplification factor.

Training a learner algorithm requires a training pool of objects that specifies the correct and incorrect object examples. In our case the pool consists of bubbles' examples and other image features that look like bubbles but are not. The next step of training a learner algorithm is introducing the training pool as a useful type of data to it, which means the training pool should be converted into its image feature information. Now the algorithm can be trained based on the prepared training data. The last step is assessing the performance of the learner algorithm to see if it creates reliable results. Now the algorithm is ready to be implemented to the detection model. The outcome of the detection process should be screened to remove the over detections and to save the true cases.

To train a machine-learning algorithm, two sets of training data were provided to the algorithm, the true and false examples of the object of interest. In our application, we wanted the algorithm to find and detect bubbles, so we collected two training pools of true and false bubble examples. Each of these pools contained more than 1400 samples. It is recommended that the false samples be as similar as possible to the true samples, so the algorithm generates a stronger decision making strategy (Dalal and Triggs 2005). Examples of training data are shown in Figure 2-10.

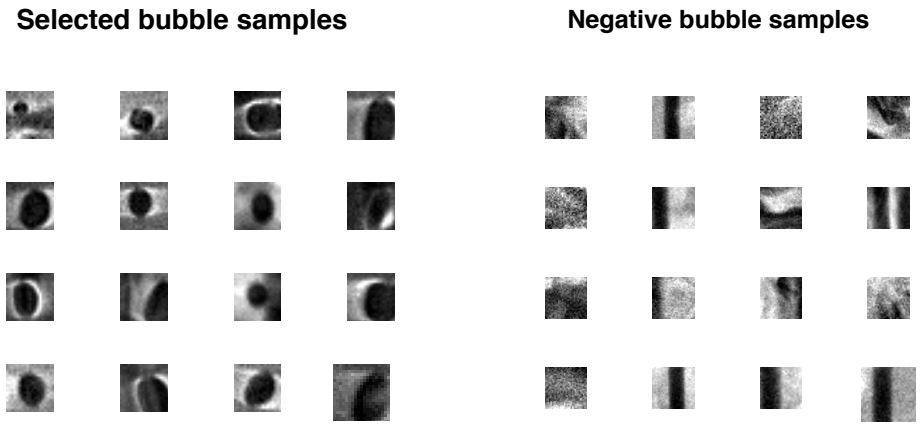

Figure 2-10 Samples from training samples for classifier

Training a classifier requires introducing characteristics and features of the object of interest to the machine (Gall et al. 2012). In the case of object detection in an image, these characteristics are the visual features of the object, such as corners, edges, or its color composition. There are various methods available for extracting visual features from a digital image such as Binary Robust Invariant Scalable Keypoints (BRISK)(Leutenegger, Chli and Siegwart 2011), Speeded Up Robust Features (SURF) (Beier and Neely 1992), Maximally Stable Extremal Regions (MSER)(Matas et al. 2004) and Histogram of Oriented Gradients (HOG) (Dalal and Triggs 2005).

Of all the aforementioned visual feature extraction methods, only HOG is capable of extracting necessary visual features of bubbles using detailed gradients, small-scale orientation binning, and large-scale spatial binning. Because of this, we used the HOG features in our detection method based on the visual characteristics of bubbles. In order to have a comprehensive descriptive feature array of a bubble, the parameters of the extraction method were tuned to best fit our data. These parameters include the cell size and block size,

which cell is a group of pixels that the histograms of oriented gradients are calculated for it. A block consists of 4 cells where the calculation is performed for each block. The other controlling parameters are the number of rotational bins and their range. We tried different parameter values, and the best result was achieved by 18 numbers of bins in the range of -180 to 180 degree.

Feature arrays from the training pool should have the same size to train a classifier. Variation in bubble sizes in our dataset caused the selected samples to be different in size. This resulted in feature arrays with different sizes for each sample. Correcting for this problem, we averaged the size of samples in our training pool and scaled all of the samples to the averaged size, so the extracted features from each sample had the same size.

To construct the decision-making strategy, different types of classifiers are available. One way to categorize these classifiers is based on the number of classes that they can classify. Algorithms like random forest (Breiman 2001) are capable of generating decision trees in order to classify large numbers of data groups (Gall, Razavi and Van Gool 2012). Sample classifiers such as Linear Discriminant Analysis (LDA) (Scholkopft and Mullert 1999), decision trees (Quinlan 1986), and Support Vector Machines (SVM) (Hearst et al. 1998, Schölkopf and Smola 1998) can classify only one or two groups. In our application, we wanted to distinguish bubbles from the rest of the components in an image; we just wanted to classify two groups in our dataset. For this reason, we used the SVM classifier. This selection was based on the fact that SVM classifiers are more robust compared to other types of classifiers (Bartlett et al. 2005, Bartlett et al. 2004).

The Support Vector Machines can be used when there are exactly two groups of data. The SVM classifies the data by constructing a hyperplane that separates the two groups. The best hyperplane is the one that creates the largest margin between the two groups and has no data point in the margin. The margin is defined as the maximal gap between the support vectors, which are the data points from each group of data that are closer to the constructed hyperplane. Matlab has a built-in SVM classifier that can be used for this purpose.

The controlling parameters of the SVM classifier in Matlab are the kernel function, polynomial order, “boxconstraint”, solver routine, and “crossval”. The kernel function defines how to construct the hyperplane. If the kernel function was specified as polynomial, the polynomial order option is used to determine the function order. The “boxconstraint” specifies the imposed penalty for false classification. The solver routine defines the solving method of the kernel function, and “crossval” gives the user the option of validating the constructed decision tree based on a portion of the provided data to the classifier.

The performance of the classifier under the provided training data with different values for the options of the classification can be seen in the Figure 2-11.

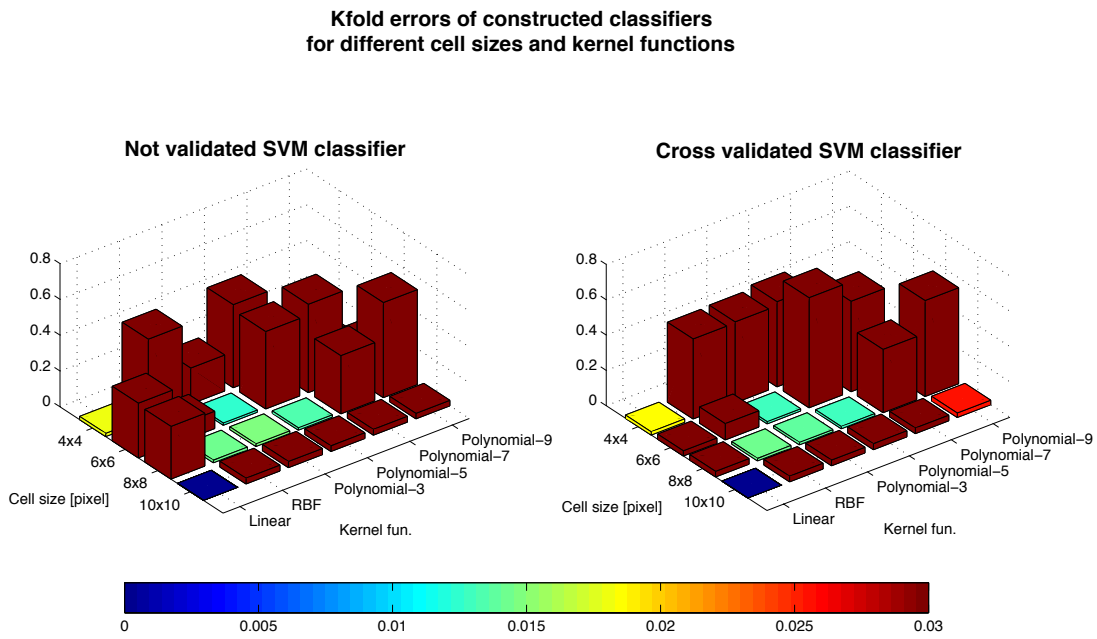

Figure 2-11 Kfold loss of the trained SVM classifier

Based on the graph in Figure 2-11, the optimized SVM classifiers in our application used a polynomial kernel function of order of 5 and the solver for the kernel was L1QP. The "boxconstratint" option was set to infinity, which means that no false decision is accepted. We used the cross validation option to improve the final constructed hyperplane of the function. Now we have all the required tools for detecting bubbles in our data set. The next step is running the classifier over each image to detect bubble instances. To do so, a sliding window technique was used (Wojek et al. 2008). In this process a window as the same size of the bubble samples in our training data pool was scanned over an image and each window was examined if it contained a bubble or not. An overlap was considered in order to create a thorough investigation. To detect the different size of bubbles, each image was inverse scaled based on stored scaling factors derived from training samples preparation. The raw result of detection process is shown in Figure 2-12.

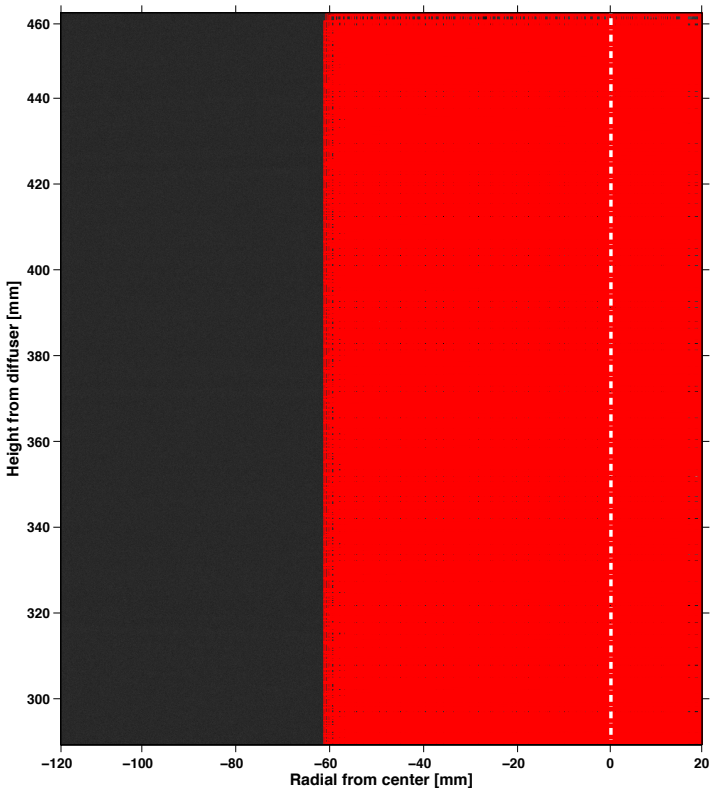

Figure 2-12 Raw detection result from the SVM classifier

It is clear from Figure 2-12 that the number of detected bubbles is not a true prediction for actual population of bubbles in the image. The reason for this outnumbering is multiple detections of the same bubble in different windows and different scales of the image. To remove repeated bubble detections, the non-maximum suppression method (Neubeck and Van Gool 2006) was applied on the results from the detection process. In this method the returned detection score and allowable amount of overlap of adjacent instances were used to find the most accurate bubble instance among multiple detections of a bubble. We tuned the function to consider the instances that had a detection score of 0.55 or higher and the allowable overlap was chosen as 25 pixels. These numbers are derived based on evaluation

tests performed to examine the efficiency of the method. The final result of the detection method after screening for the true detections is shown in Figure 2-13.

To calculate the void fraction ratio in our data set, for each case of bubble flow rate the derived map of presence of bubbles was used in Equation (2-3). As can be seen in the picture, actual bubble instances occupied a portion of the detection windows and it was not possible to calculate the correct area of each bubble from this data. To address this discrepancy, the averaged ratio of the bubble size to the detection window was calculated. For this matter, the area of each bubble instances was measured manually and compared to the area of the related detection window. This measurement showed that the averaged ration of occupied area of a detection window by a bubble is r=0.18.

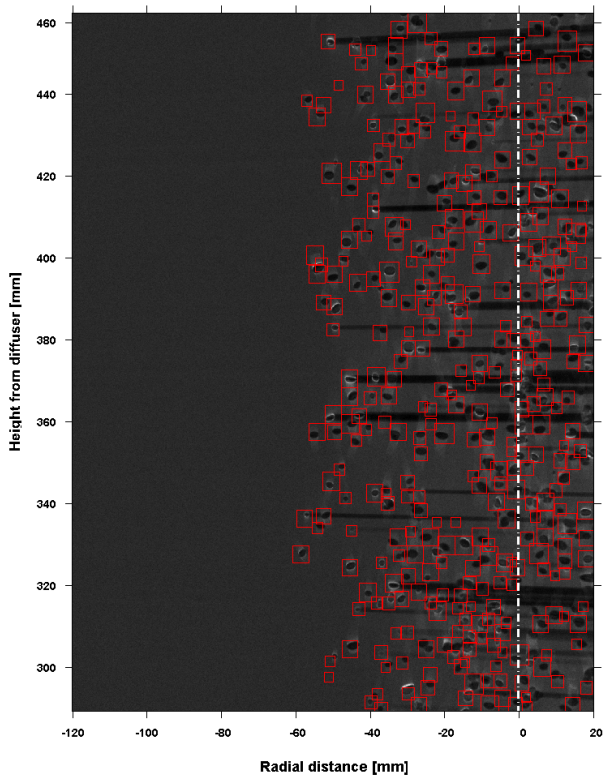

Figure 2-13 Screened detection results by the NMS method

We applied this correction ration to Eq. (2-3) to derive a true probability of bubble presence. One further step toward creating a precise probability map of bubbles, we calculated the probability of presence of a bubble in a 2x2 block size. Each block contained 4 windows with known bubble presence probability. The ensemble of these values over the block was considered as the bubble presence probability in each block. The final results are shown in Figure 2-14. We compared the values of Figure 2-14 with the findings of Seol, Bhaumik, Bergmann and Socolofsky (2007), which was the local time-averaged void fraction at the range of 0.7%-1.8%. Our values are about 10 times higher. This is due to difference in the counting method we used in our technique comparing to their method.

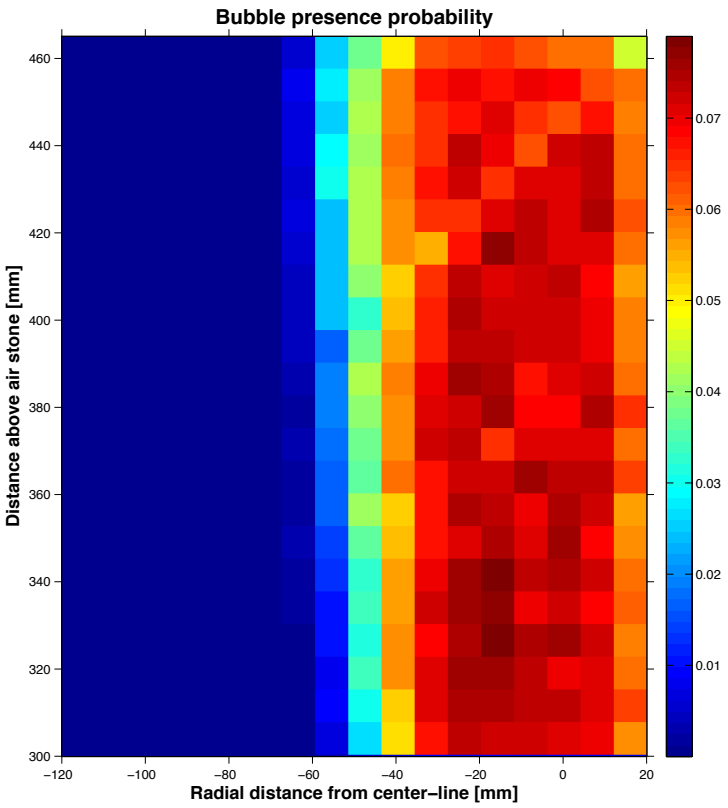

Figure 2-14 Bubble presence probability

Figure 2-15 shows the flow chart for the process of detecting and calculating the probability of presence of bubbles in the plume.

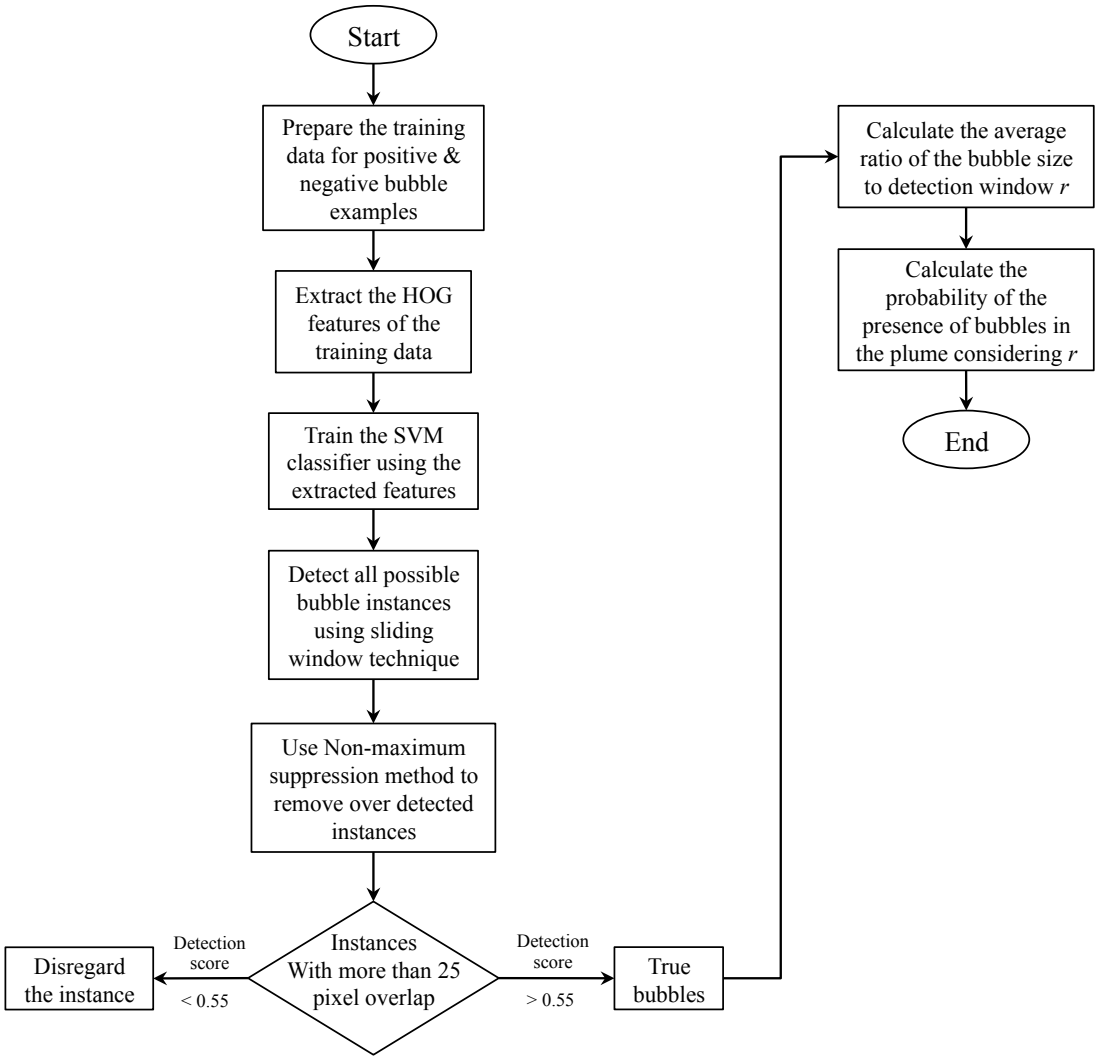

Figure 2-15 Bubble detection flow chart

Based on the calculated presence probability of bubbles, we used the uniform dye concentration experiments and Eq. (2-4) to evaluate the intensification factor of bubbles, which resulted in a_v = 3.848e-3 1/pixel. This value is comparable to the value calculate by Seol (2008) that was a_v = 9.576e-3 1/pixel with differences dye to using a different laser and void fraction method. Applying this factor to the recorded data for the uniform dye concentration experiments, we could mitigate the intensification factor of bubble presence.

The corrected intensity profile is shown in Figure 2-16. The error bars on the graph are the standard deviation of intensity values of each pixel over the duration of the experiment. In the case of 3 μg/l, the intensity values at the edge of the bubble core still show the effect of bubble intensification even after the correction analysis, but it is limited to the edge of the bubble core, and the true concentration is within the error bound.

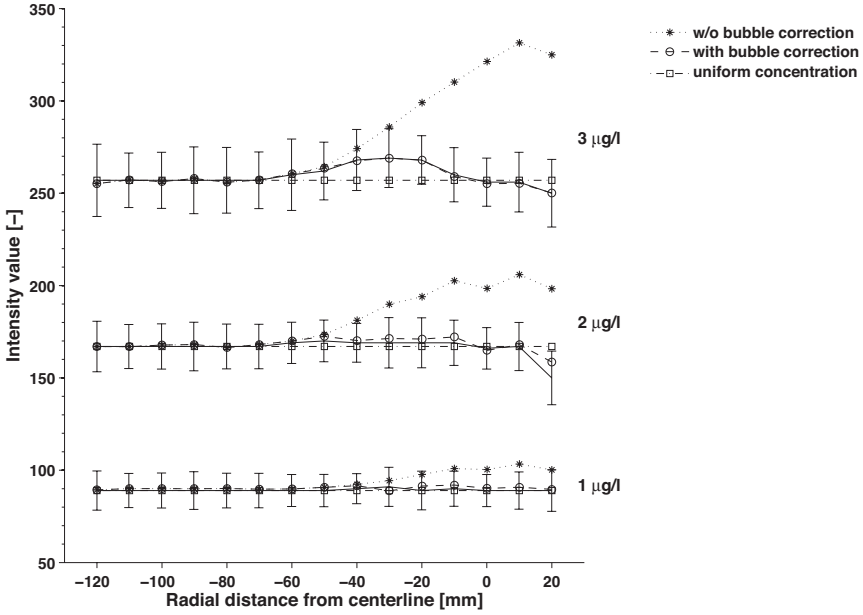

Figure 2-16 Corrected profile for bubble intensification

2.4 Conclusion

In this chapter a novel image processing technique was introduced for analyzing the recorded images by the 3DLIF technique from a multi-phase plume. In this method, bubble and shadow signatures were detected automatically based on their intensity characteristics and removed from the image. Furthermore, the hotspot pixels were removed using the intensity value difference ratio of original and smoothed images. Further, the effects of the presence of bubbles on the light sheet intensity in the plume area were corrected. To account for the

bubble presence, the machine-learning algorithm was employed to detect bubble instances. Knowing the number of bubbles enabled us to calculate the bubble presence probability in our bubble plume. Using this information, we were able to correct the reflection effects of bubbles.

3 IMPLEMENTATION OF THE 3D-PLIF TECHNIQUE INTO MEASUREMENT OF THE CONCENTRATION FIELD INSIDE OF A MULTI-PHASE PLUME BY ACCOUNTING FOR THE PRESENCE OF BUBBLES

3.1 Introduction

Buoyancy or momentum driven flows, such as deep-water thermal vents, volcanic eruption, air bubbles plumes for lake restoration, disturb their surrounding environment by mixing and displacing the components of the environment. Studying the mixing properties of these flow structures requires measuring the concentration field inside them. Various intrusive and non-intrusive measurement techniques have been applied to accomplish this measurement. One of the non-intrusive methods is the Planar Laser Induced Fluorescence (PLIF) technique. This method was developed and tested for single-phase flows, resulting in what is now a standard measurement technique. To expand the measurement domain, the PLIF technique has been expanded into the 3D-PLIF technique by scanning multiple 2D slices. These measurements have not been performed on a multi-phase flow and new corrections are needed to account for disruptions by the dispersed phase. In this chapter, we adapt the 3D-PLIF technique to study the mixing properties and to measure the concentration field of a bubble plume.

Studying the mixing process and flow characteristics of different environmental processes requires measuring the concentration field inside of those flow fields. The preliminary tools for this measurement were physical probes; examples include: hot-wire anemometry (Bruun 1996, Libby and WAY 1970), fiber optics (Cartellier and Achard 1991, Herbert et al. 1994), needle resistivity probe (Chanson 2002), and conductivity probes (Revankar and Ishii 1993, Wu and Ishii 1999). Inserting these probes in the stream of a flow creates disturbance in the

natural condition of the flow. To avoid imposing artificial structures in the flow, the number of implemented probes were restricted resulting in a limited amount of collected data. The next generation of measurement methods was non-intrusive methods like the Laser Induced Fluorescence (LIF) technique that avoids disturbing the flow condition. In this method, a tracer is injected into the flow field that tracks the flow structure and mixing properties of the flow and the fluorescence of the illuminated tracer is then captured by the camera system used in the test. Koochesfahani and Dimotakis (1985) was able to visualize the vortical structures of mixing layer and qualitatively interpret the mixing properties of the shear layer flow by implementing the point-wise LIF technique.

The early setup of the LIF technique consisted of a single laser beam as the lighting source and an array of photo diodes as a recording apparatus. Using optical lenses and scanning mirrors helped to expand the measurement area from a ray to a plane. With this configuration, a bigger area of flow was visible to the recording device. Therefore, the amount of collected data in time was increased compared to the point-wise measurement. Ferrier, Funk and Roberts (1993) conducted the Planar Laser Induced Fluorescence (PLIF) experiment to measure the flow properties in mixing fluids. As a part of their research, they explained calibration steps that are required for an accurate flow measurement. To study the simultaneous mixing and turbulence of a turbulent jet, Cowen, Chang and Liao (2001) designed a concurrent experiment of the PLIF and Particle Image Velocimetry (PIV) technique. They were able to extract the concentration map from the PLIF data and turbulent scalar flux of the flow by analyzing the synoptic PIV velocity field data.

To study the spatial and temporal scalar structure of a turbulent plume, Crimaldi and Koseff (2001) developed a new correction and conversion method for the PLIF technique to convert the intensity values into the concentration data. They measured the background concentration at the beginning and the end. Assuming a perfect mixing process by the flume flow, they linearly interpolated the background concentration for each step of measurement. Also, they showed that the produced amount of error due to neglecting the attenuation effect of tracer dye for the concentration values below 2ppm is less than 1%. Hence, they did not consider this correction in their analyses to reduce the computational cost and increase the speed of the process.

The necessity of studying the whole width of a flow structure pushed the PLIF technique to expand in the third dimension and become the 3D-PLIF technique. Tian and Roberts (2003) used the technique to study the concentration field inside of a vertical turbulent jet in a cross flow. They collected more data with this method compared to the PLIF technique, which yielded more insight into the mixing properties of the flow. Gandhi, Roberts, Stoesser, Wright and Kim (2011) studied the mixing process of flow around the UV lamp in water disinfection facilities by using the same method. They resolved the 3D map of flow structure and the exposure time of the flow to the UV rays.

Reviewing the available literature in the field of concentration measurement and the mixing process of environmental flows shows that most of these efforts were focused on the single-phase flows, whilst there are many types of multi-phase flows that require research and investigation to understand their flow structure and mixing properties. One of the examples of multi-phase flow is an air bubble plume. Seol (2008) conducted an initial investigation on

the concentration field inside of a bubble plume using the PLIF technique by accounting for the presence of bubbles. The issue of the PLIF technique with the multi-phase flows composed of components with different refractive indexes is the light reflection from the surface of immiscible particles. It causes uneven lighting over the field of view of an experiment and results in biased interpretation of data. To address this concern, Seol (2008) showed that the excess amount of illumination is related to the probability of the presence of bubbles. With this assumption and applying the corresponding corrections, He was able to accurately resolve the concentration map inside of a bubble plume.

In this research, we expanded the developed method by Seol (2008) to the 3D-PLIF technique. We wanted to measure the concentration field inside of a bubble plume to study the mixing process and its concentration field. In our experiments, we used a collar injector to add Rhodamine 6G as a tracer dye into the flow field and illuminated it by the laser light. We applied the correction method developed by Crimaldi and Koseff (2001) and Seol (2008) to extract accurate quantitative concentration results. To address the presence of bubbles in the recorded data, we developed a new autonomous method to detect and remove the bubbles and calculate the probability of presence of bubbles in the field of view. The resulting data provided insight on the mean and turbulent fluctuating concentration field.

This chapter is organized as follows. The setup of our experiments is explained in part 2, in part 3 the correction calculation and analysis methods are presented. Part 4 contains the results conclusions and a detailed discussion is in part 5.

3.2 Experimental set-up

All the experiments were performed in a glass walled tank, 2 m long, 1.5 m wide and 1.1 m deep in Fluid Dynamics Laboratory in the Zachry Department of Civil Engineering at Texas A&M University. The tank was filled with water purified by reverse osmosis method in order to prevent any chemical reaction of fluorescent dye with the chemical components of tap water. The depth of water in the tank was kept constant during all experiments at 0.95 m. The source of the air bubble plume was a cylindrical aquarium air stone, 14 mm in diameter and 20 mm in height. The air stone was placed at the bottom of the tank with equal distance of 500 mm from the front and sidewalls. The produced bubbles' diameter was in the range of 0.5-4 mm with the volume median diameter of $D_{50} = 2.4$ mm. The airflow was controlled by a mass flow meter at the prescribed flow rates.

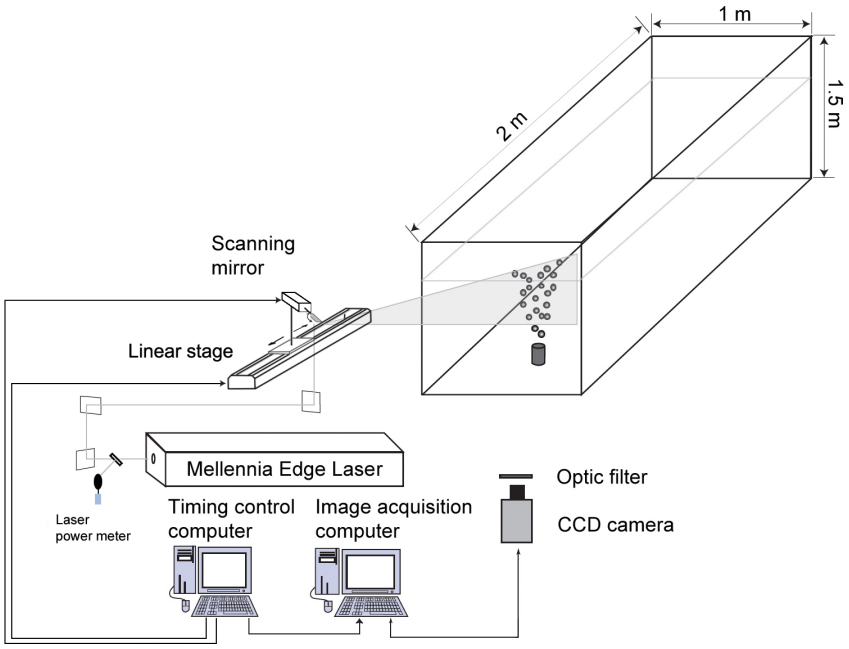

Figure 3-1 3D-PLIF experiment set-up

The laser source was a 5-Watt solid-state continuous wave Nd:Yag green laser with 532 nm wavelength (Spectra-Physics Millennia Edge Single Frequency CW). The laser beam was directed into the tank through optical mirrors, and a fast galvanometer-scanning mirror (Model 6220MH60, Cambridge Technology, Inc.) was used to create a laser sheet. A Coherent FieldMaxII-TOP power meter measured the laser power fluctuations during experiments. About 10% of laser light power was directed into the power meter by a standard microscope slide (Cowen, Chang and Liao 2001).

The fluorescent dye that we used in these experiments was the Rhodamine 6G. The peak absorption wavelength of Rhodamine 6G in water is 524 nm and it emits light at the 555 nm (Crimaldi and Koseff 2001). Its strength against photobleaching makes the Rhodamine 6G a good choice to be used in a quantitative study of the concentration field. The injection system of the fluorescent dye consisted of a Mariotte bottle and a collar injector that was placed right above the plume source.

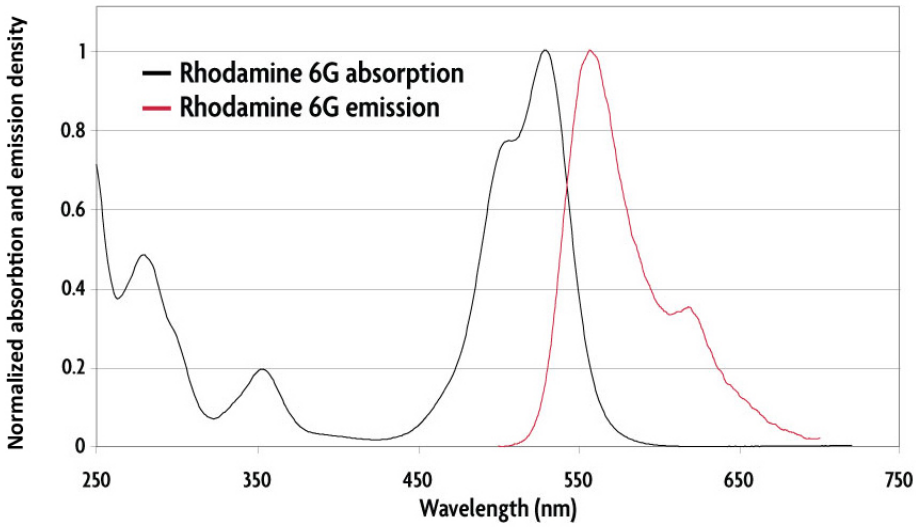

Figure 3-2 Rhodamine 6G absorption and emission spectrum

A high-resolution CCD camera (Flow Master 3S, 12 bit intensity depth with 1024x1280 pixel resolution) was used to capture the fine-scale details of the plume structure. The highest recording frequency of the camera was 4 Hz. The camera was equipped with a Nikkor 35 mm focal length lens and controlled by the Davis 8.1.2 software from LaVision. The exposure time of the camera was set to 25000 μs, long enough for the laser beam to scan one slice over the whole area of the field of view (FOV). To filter out the laser light from the emitted light by the fluorescent dye, a 543 nm cut-on filter (543AELP, Omega Optical, Inc.) was installed on the camera lens. The FOV of these experiments was a 175 mm by 140 mm rectangular plane, and the bottom of the FOV was 295 mm above the source of the bubble plume.

To create a 3D profile of the concentration field, the scanning mirror was mounted on a motorized linear stage (A-LST0750B Zaber technologies Inc.). With this set-up, the laser sheet remained perpendicular to the camera axis at all times.

To synchronize the camera, scanning mirror, and the linear stage, we used LabView software. The synchronizing signals are shown in Figure 3-3. During the oscillation of the scanning mirror, the linear stage was kept stand still and the camera shutter was open. The oscillating function of the scanning mirror was made non-linear in order to create a uniform lighting over the FOV (Crimaldi and Koseff 2001).

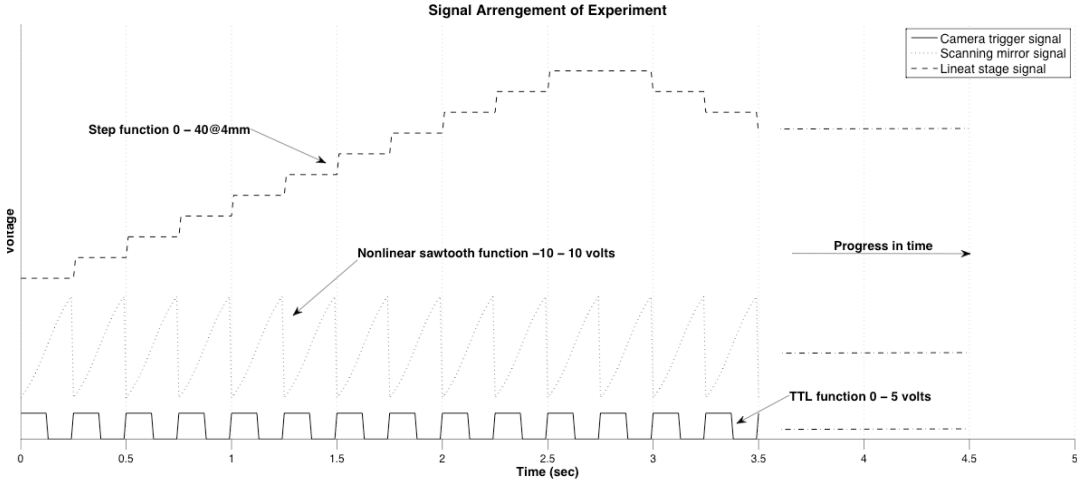

Figure 3-3 Synchronized triggering signal for 3D-PLIF experiment

At the FOV height, the diameter of the plume was about 80 mm. Based on the axis-symmetry characteristic of the bubble plume, we captured the concentration field for half of its width. Therefore, the movement range of the linear stage was set to 40 mm at 4 mm steps to cover a wedge containing 1/4 of the plume. With this setup, we recorded 11 slices over the half width of the plume. To capture clear pictures over the course of laser sheet traverse, the aperture of

the lens was set to f2.8. The camera was focused at the centerline of the plume. With this aperture we had a clear view over the width of the plume in front of the centerline of the plume. In order to capture the ongoing events at the edge of the plume, the plume centerline was aligned 20 mm from the right side of the FOV. Note: the plume centerline is identified in each of the results fields presented in sections 3.4 and 3.5.

3.3 Calibration tests and correction analysis

We adapted the conventional correction procedure of laser light attenuation from Ferrier, Funk and Roberts (1993) and Crimaldi and Koseff (2001). In this procedure, the attenuation of laser light is correlated to the path length of laser beam in water, a_W, and to concentration of tracer dye in water, a_d. In the case of multi-phase plume, the presence of immiscible particles is the new source of disturbance requiring correction. For addressing the presence of bubbles in our data, we followed the method developed by Seol (2008) to calculate the correction coefficient of bubbles presence, a_v. The combined attenuation coefficient is as:

$$a = a_W + C \cdot a_d + \alpha \cdot a_v \qquad (3\text{-}1)$$

Where C is the tracer dye concentration and α is the probability of presence of bubbles in the plume. The first calibration test measured the power attenuation of laser by water. As the laser beam travels in a denser medium like water, its power reduces and as a result, it cannot create uniform illumination over the FOV. To measure the amount of attenuation of laser power in water, a glass bottle filled with 0.02 mg/l solution of the tracer dye was placed at incremental steps from the light source in the FOV. The pictures of the bottle illuminated with 5-watt laser light were recorded for further calculations. Depicting the intensity values

of the bottle against corresponding distances and fitting an exponential curve to the scatter points gives us the water attenuation factor for laser power. The resulting curve and calculated water attenuation factor for our experiments are shown in Figure 3-4.

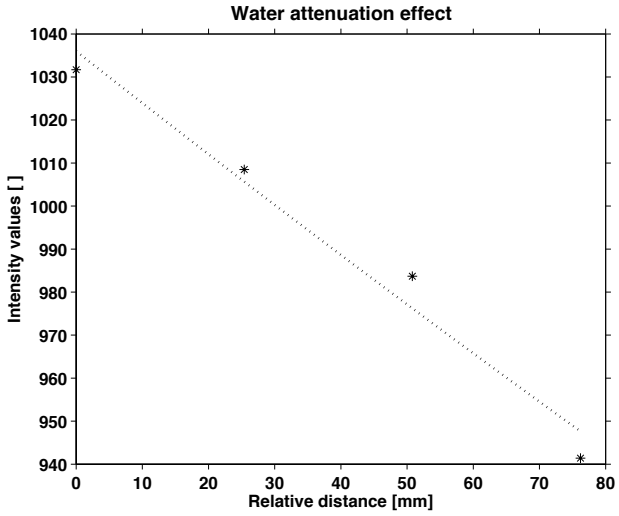

Figure 3-4 Water attenuation effect on image intensity

Based on this calculation, the power attenuation factor of laser in water in our experiments was a_W = -1.04e-4 1/pixel. Injecting a tracer dye into the plume creates a new source of energy attenuation for the laser power. Crimaldi and Koseff (2001) found in their experiments that the presence of tracer dye in the field of view with concentration values less than 2 ppm causes less than 1% error in the final results of the experiments if the effect is neglected. They stated that in order to speed up the post processing analysis of a PLIF experiment they would not consider this correction. In our experiment, benefiting from the high power laser source capable of producing 5-Watt output, we reduced the concentration of the tracer dye solution without compromising the clarity of recorded data to the values below 2 ppm and we were able to assume that a_d=0. Once the dye was injected into the rising

plume, the mixing process of the plume diluted the tracer solution to the concentration amounts much less than 2 ppm, which resulted in negligible amount of attenuation from the tracer dye.

The PLIF and 3D-PLIF techniques require converting the recorded raw intensity data into concentration values. To perform this conversion, the correlation factor of intensity and concentration should be measured by a calibration test. In this test, images of a glass bottle filled with different concentration of tracer dye solution were captured at a fix position. The bottle was illuminated with a constant laser power during the test. Ferrier showed that the Rhodamine 6G has a linear response to the laser light for concentration values below 50 μg/l. In our test, we used 10, 20, and 50 μg/l tracer dye solution to derive the conversion factor of intensity to concentration. Figure 3-5 shows that the Rhodamine 6G has a linear response to the laser light for the selected concentration values. The calibration result obtained for our experiments was:

$$C(i,j) = 1.676e^{-5} I_c(i,j) + 4.843e^{-4} \qquad (3\text{-}2)$$

Where, *C(i,j)* is the concentration value in mg/lit at each *(i,j)* pixel, $I_c(i,j)$ is the corrected intensity data.

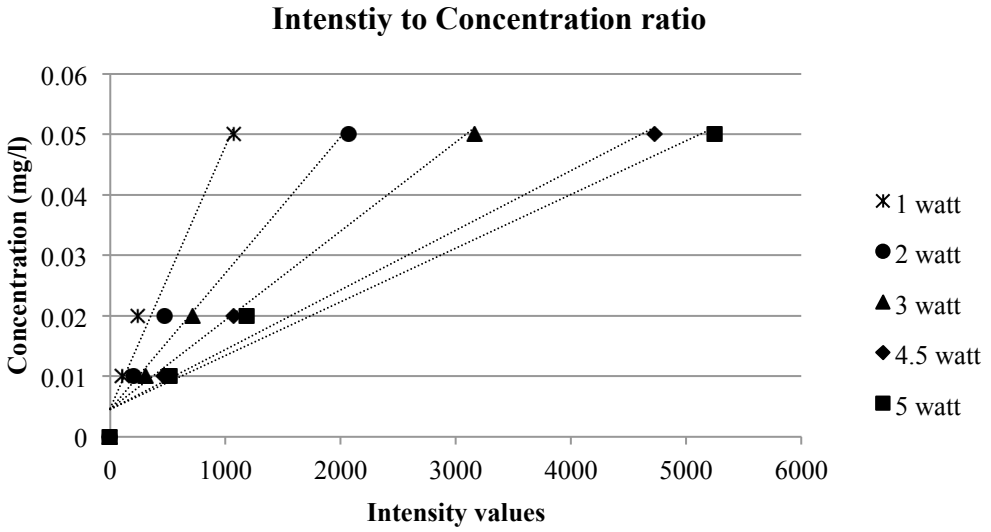

Figure 3-5 Rhodamine 6G response to light

To keep track of the amount of injected dye into the tank, the injection time of the dye solution was recorded. With this recording, the concentration of dye inside of the tank is known at the beginning and the end of an experiment. To extract the background intensity for each image the average intensity of the bottom left corner of the image over an area of 150 by 150 pixel was calculated. The calculated value is considered as the background intensity for the specific image.

The vignette effect is another optical deficiency of the 3D-PLIF technique that should be corrected. This effect is the result of receiving less light by the corner areas of CCD chipset of the camera due to the rectangular shape of the chipset compared to the circular shape of the camera lens. Tian and Roberts (2003) proposed a method to correct the effect by means of a standard image. They performed this correction following the Eq.(3-3).

$$I_C(i,j) = \bar{I}_S \frac{I_R(i,j) - I_D(i,j)}{I_S(i,j) - I_D(i,j)} \tag{3-3}$$

Where the $I_D(i,j)$ is the camera dark response, $I_S(i,j)$ is the recorded standard image from a uniformly illuminated white surface, $I_R(i,j)$ is the corrected image for attenuation effects, and $\bar{I}_S$ is the average intensity value of the standard image. Since the standard image is recorded under different condition than the original experiment, the captured vignette effect by the standard image would be different than the one in the data from original experiments.

To address this problem, we developed a new correction method based on the original experiment data. We know that the image of a uniformly illuminate area should have a uniform intensity values after correction for the vignette effect.

$$I_C(i,j) = const. \qquad \text{for any } i,j \text{ in the field of view} \tag{3-4}$$

We created the uniformly illuminated area by adding negligible amount of dye into the tank, enough to be visible to the camera with signal to noise ratio higher than 5 comparing to black response of the camera chipset. In this method, instead of getting to the corrected image from vignette effect, we made an arbitrary final result. Following the back calculation based on the Tian and Roberts (2003) method, the only unknown parameter would be the standard image. Based on this process, not only we were able to correct the vignette effect of the camera lens but we could do so under the same light conditions as the original experiments.

$$I_S(i,j) = \bar{I}_S \frac{I_R(i,j) - I_D(i,j)}{I_C(i,j)} + I_D(i,j) \tag{3-5}$$

Here, $\overline{I}_S$ can be any arbitrary number as it will be canceled out in the original equation. The standard image calculated based on our method and the one recorded by the conventional method can be compared in Figure 3-6 and the corrected image based on each of these images is shown in Figure 3-7.

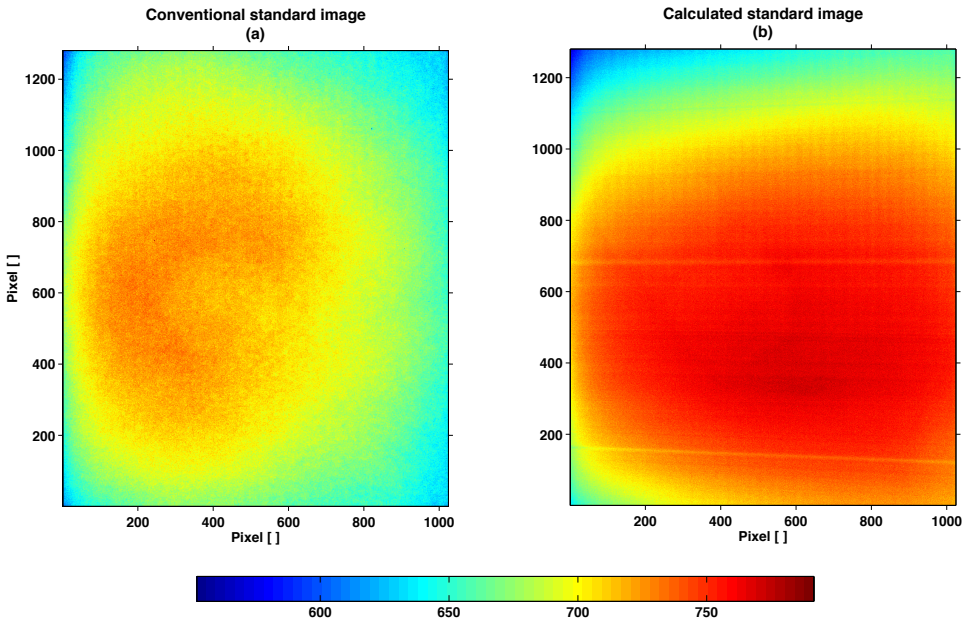

Figure 3-6 Comparing calculated and conventional standard images

Figure 3-6 shows the vignette correction using the standard method (a) and the methods proposed here (b). In the standard method, the correction is less uniform due to the difficulty to uniformly illuminate the image background (we used front lighting on a white plane). Figure 3-7 shows the results of applying our vignette correction from Figure 3-6(b) to data from a PLIF image in uniform dye concentration. Figure 3-7(a) is the PLIF image before vignette correction, (b) shows the vignette correction filter, and (c) shows the PLIF image after vignette correction. The intensity variation across (c) is near the noise threshold of the camera; hence, we conclude that the vignette correction has succeeded.

3.4 Corrections in multiphase flow

Each of the preceding image corrections are standard in single-phase applications of the PLIF method. In a multiphase flow, we must also account for the presence of the bubbles. This requires two main corrections: we seek to remove the bubble signatures so that we obtain data for the dye only and we must account for changes in the laser illumination due to the presence of the bubbles which have a different index of refraction compared to the water. The first thing that makes a difference between single and multi-phase flows is the presence of immiscible components in the flow field. A tracer dye can freely move all over the flow field of a single-phase flow however in the case of multi-phase flows, the immiscible components are barriers for the tracer dye motion in the flow field. Under this circumstance, the intensity values of the immiscible particles are not the true representative of the presence of dye in those positions. For this matter, detecting and removing the signatures of the immiscible components from the recorded data is necessary for extracting accurate quantitative results.

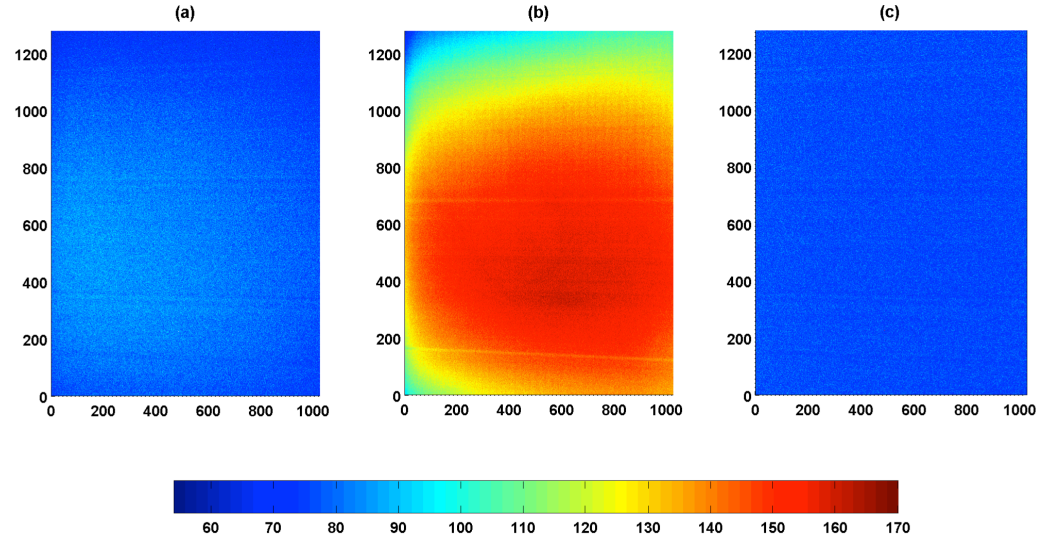

Figure 3-7 Vignette correction

The second effect of immiscible components of a multi-phase flow on the results of 3D-PLIF experiment is creating an uneven amount of lighting in their vicinity. The laser beam may reflect from the surface of those particles in any arbitrary direction. The reflected laser light by particles in the same surface of the laser sheet adds extra lighting energy to the illuminated area that in result, creates higher intensity values in the recorded data. Intensity values are correlated to the concentration of the tracer dye, so any change in the intensity value is interpreted as a change in the dye concentration, which in this case is not true. To address this ambiguity, Seol (2008) proposed a correction method based on the void fraction ratio in the plume. He related the averaged intensity image to the void fraction map multiplied element wise by the radius map of the image to extract the intensification factor of bubbles, since they increase the light energy.

The void fraction is defined as the ratio of the presence time of bubbles in specific point to the total observation time.

$$\alpha(i,j) = \frac{\sum_{i,j} t_G(i,j)}{T} \tag{3-6}$$

Where, $t_G(i,j)$ is the amount of time that the bubble presents in pixel (i,j) and T is the total time of an experiment. To calculate the void fraction, Seol (2008) manually detected bubbles and categorized them with respect to their size into two groups, then applied two different filter sizes to remove and count bubbles. It was possible for him to do this because the number of images in his data set was limited, and bubble sizes were not varying in a broad range. In our experiments, the number of images are larger compared to his dataset, and bubble sizes ranged from 0.5 to 4 mm with the d_{50}=2.5 mm based on our previous measurements. With this type of data, the only practical method is an autonomous analysis. For this matter, we developed a detection and removal method based on the shape and intensity values of bubble instances using the machine learning techniques.

In this method, which is explained in more detail in chapter 2, we trained a support vector machine (SVM) classifier to detect bubbles in our dataset. The dataset that was used for calculating the void fraction were images with uniform tracer dye concentration. After a detection process, the classifier returned the approximate size of a bubble and its position in an image. An example of detected bubbles in an image is shown in Figure 3-8.

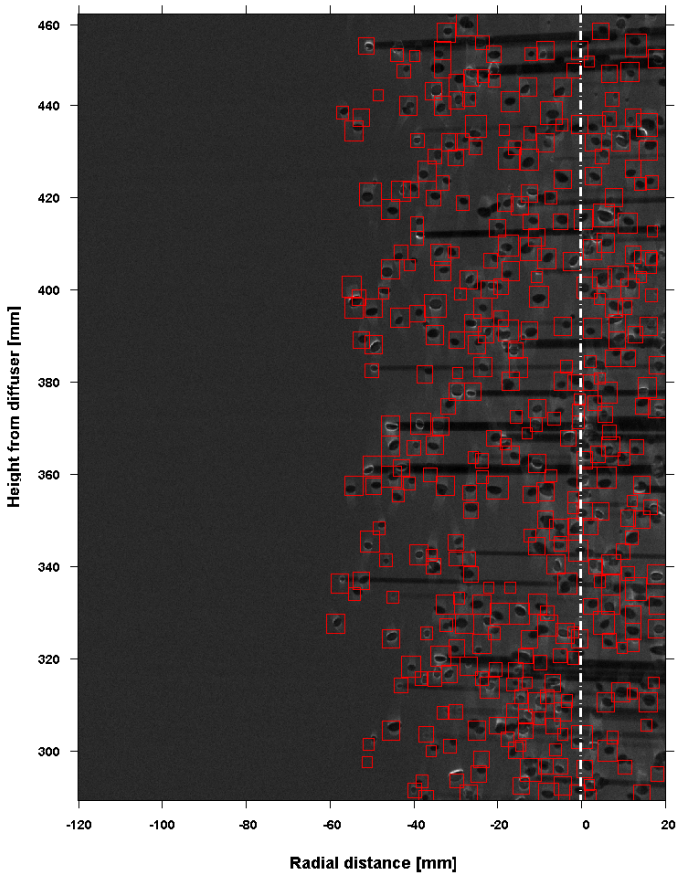

Figure 3-8 Detected bubbles by SVM classifier

The bubble information was then screened to remove overlaps and double detections. The final result of the detection process was used to calculate the void fraction ratio following the Seol (2008) method. The void fraction map in our data set is shown in Figure 3-9.

By knowing the void fraction of our plume, we calculated the laser intensification of bubbles in our experiment as a_v = 3.848e-3 1/pixel.

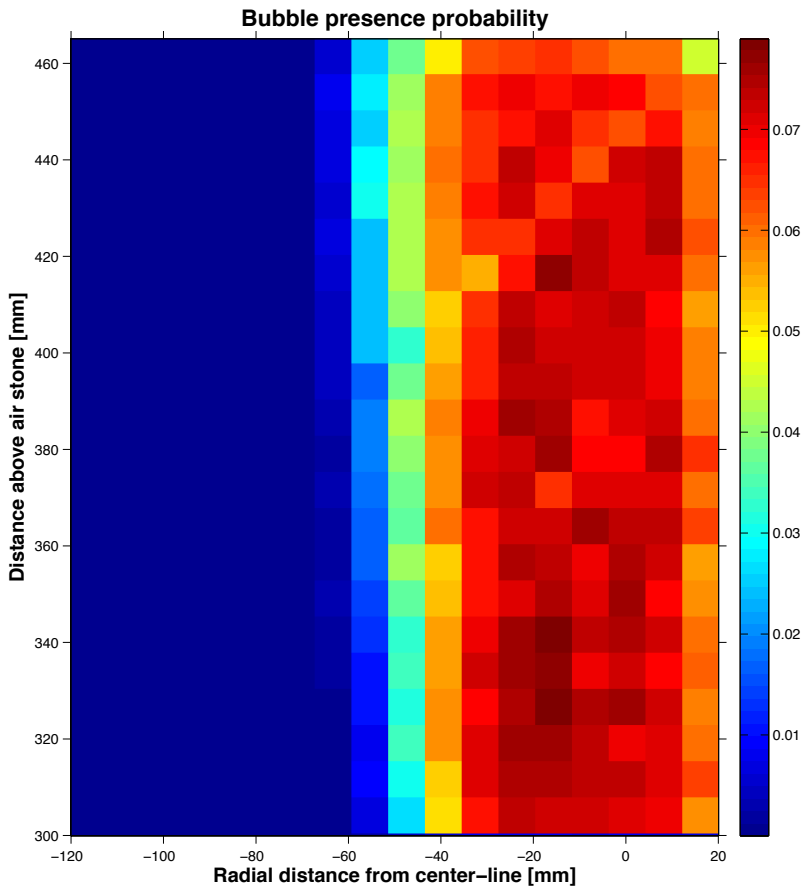

Figure 3-9 Bubble presence probability

Using the calculated bubble intensification factor and the bubbles presence probability, we could correct our data set for the bubble intensification effect. The results are shown in Figure 3-10. This figure shows that the original profile of the intensity values rises in inside of the plume body due to the intensification effect of bubbles. But after applying the correction factor for the bubble intensification, the intensity profile falls back on the uniform concentration profile. The error bars show the standard deviation of instantaneous intensity values over the time. The bubble intensity correction method has corrected the mean concentration result to be close to the known values except at the edge of the plume in the 3 mg/l case, where a slight bias remains. Even in this biased region, the true value falls within

the error bounds of the measurements. Error bars in all cases give the fluctuation errors due to camera noise and uncorrected reflections from the bubbles. These errors are on average less than 0.089 of the true values. This level of error is acceptable for predicting the mean concentrations and is below the large concentration fluctuations observed in tests without uniform dye concentration. Hence, the method is performing at an adequate level.

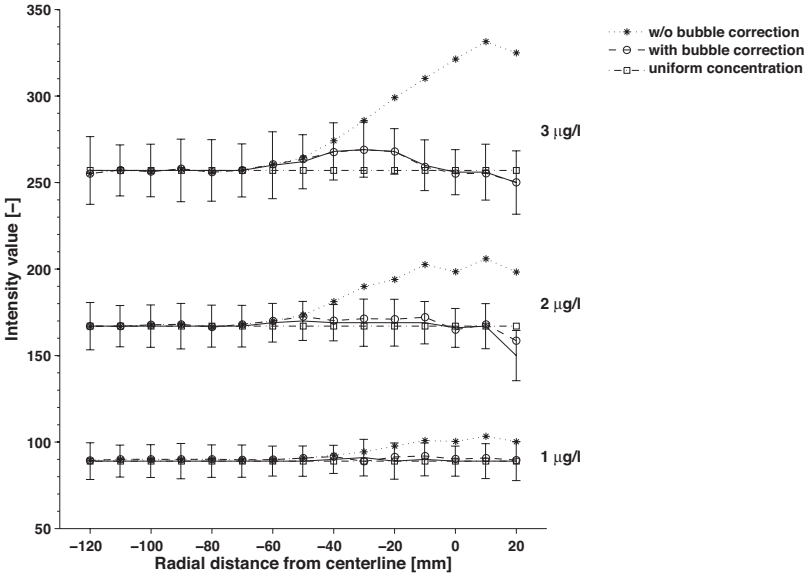

Figure 3-10 Corrected profile for the bubble intensification

Now that we have all of the required correcting parameters we can modify the recorded data using this formula:

$$I_c(r,\theta) = \frac{I(r,\theta)}{\exp\left(\int_0^r a\,dr\right)} \tag{3-7}$$

Where, $I_c(r,\theta)$ is the light intensity value of an image after final correction consisting of vignette removal, accounting for water attenuation, and accounting for the bubbles

intensification. *a* is the correction factor calculated following the Eq. (3-1). The correction process was carried out in the radial coordinate along the laser beam path. The corrected intensity value data from water attenuation, camera lens vignette, and bubble intensification effects can be converted into the concentration map. The conversion factor of intensity to concentration was calculated using Eq. (3-2).

In the next section, the results of the concentration measurement and derived flow characteristics of a bubble plume will be discussed.

3.5 Results and discussion

By applying the 3D-PLIF technique to the concentration field measurement of a bubble plume and considering the additional correction steps, we showed that the technique has promising results for this type of measurements in the field of multi-phase flows as well as single-phase. Here, we present results for dye injection using a round collar injector at the air-stone source. The constructed 3D presentation of the plume is shown in Figure 3-11. It can be seen from the image that the concentration field is not completely circular around the plume center (0,0).

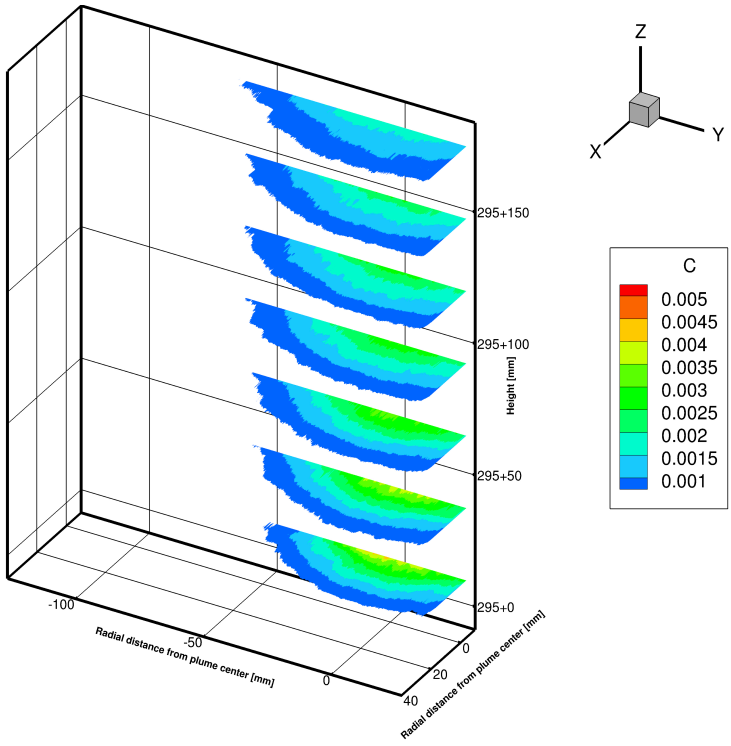

Figure 3-11 Horizontal slices of the time averaged concentration field mg/l

In Figure 3-11, three profiles of time-averaged concentration field are shown in the heights 4.5, 5.5, and 6.5 D, where D is the bubble plume length scale by Bombardelli, Buscaglia, Rehmann, Rincón and García (2007). In our experiments this length scale for the bubble flow rate of 1.0 lit/min was 0.07 m. The horizontal distance from the centerline was normalized by the plume radius at corresponding height, which were 25.4 mm, 29.1 mm, and 32.8 mm respectively. The normalized time-averaged concentration profiles show the self-similarity behavior with slightly different spreading in the x and y direction. Comparing the standard deviation of the plume in the x and y direction shows that in our experiments, the distribution of the concentration field was not perfectly circular (Figure 3-12). To check for the correctness of our measurements, the concentration values derived from the image analysis were compared to the measured concentrations during the experiment. For this purpose, we

recorded the injection time of the tracer solution into the experiment tank and we calculated the existing concentration of the tracer dye at the beginning of each set of experiment. Comparing the actual and calculated concentration values shows the calculation error is less than 5%, and in the higher intensity values, the error decreases to fewer than 3%.

This asymmetric spreading was an unfortunate product of the construction of our collar injector. Figure 3-13 shows a picture of the diffuser mounted on the air stone. At the T-junction between the dye supply line and the circular diffuser, there were a non-uniform spacing of holes so that dye was not injected perfectly uniformly around the circumference of the plume. Due to the lack of a swirl motion in the bubble plume velocity field, this non-uniform initial condition of the dye source is preserved to very high heights in a non-dimensional sense (to scales of $z/D > 6.5$), which is in the asymptotic regime of the plume and is higher than most practical positions in engineered or environmental applications of bubble plumes. Despite this shortcoming, the data in each orthogonal direction (x, and y) are self-similar and converge to the same values on the plume centerline. Hence, we continue the discussion to analyze the time-average mixing characteristics of the bubble plume.

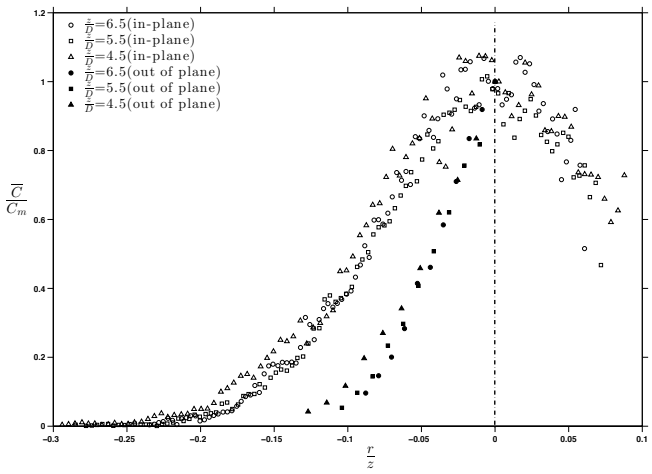

Figure 3-12 Normalized time averaged concentration

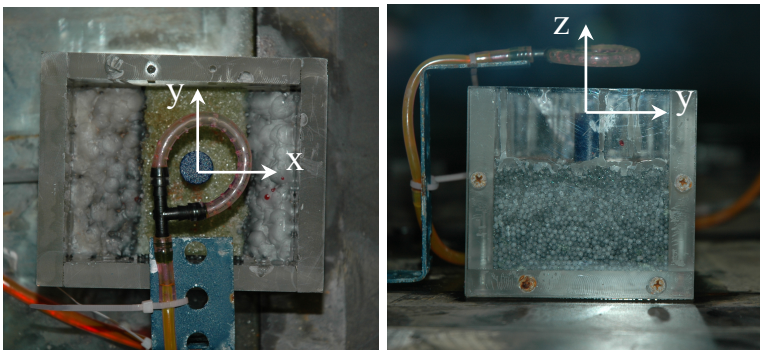

Figure 3-13 Collar injector positions

The asymmetry of the plume, which is also seen in the plume spreading rate with height, is shown in Figure 3-14.

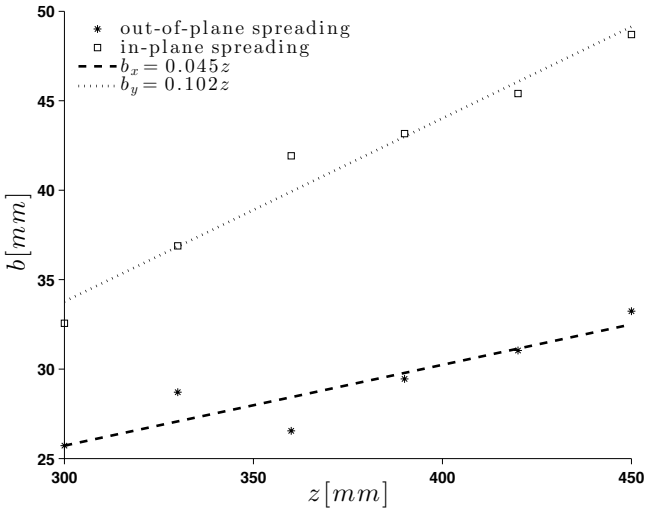

Figure 3-14 Spreading on the concentration field over the height

The spreading rate of the concentration field in the x or out-of-plane direction is much less than in the in-plane direction.

Lee and Chu (2012) showed that in the case of single-phase plume, the spreading rate is 0.105, which is close to the rate that we found for dye concentration field in the y-direction, where the dye injection was uniform. Hence, we conclude that the concentration field on the y-z plane is unbiased by the injector.

An important time-average result of the concentration field is the centerline dilution. From single-phase plume theory, we expect the centerline dilution, given by $\overline{s} = \frac{C_0}{\overline{C}_m}$, to scale with $z^{5/3}$ (Lee and Chu 2012). Figure 3-15 shows the centerline dilution versus height. The dilution is scaled by $Q_p(0)$, the initial plume water flow rate and F_0, the initial buoyancy flux of the bubble plume.

$$F_0 = \left(\frac{\rho_a - \rho_b}{\rho_b} \right) g Q_o \qquad (3\text{-}8)$$

Where ρ_a and ρ_b are ambient and bubble density, respectively, and Q_0 is the initial gas flow rate of the plume. $Q_p(0)$ was calculated using the work of Wüest, Brooks and Imboden (1992) and iterative calculations at the end of the Zone of Flow Establishment (ZFE) (Socolofsky et al. 2008). For the data in Figure 3-15, the proportionality coefficient between $\frac{\overline{s} Q_p(0)}{F_0^{1/3}}$ and z is of order 0.1, which agrees well with the single-phase results reported in Lee and Chu (2012) of 0.096. From this result, we can conclude that the net entrainment rate in the multiphase bubble plume at the measurement height is similar to entrainment rates in single-phase plumes. While it is known that entrainment rate is not constant in multiphase plumes (Seol, Bhaumik, Bergmann and Socolofsky 2007), numerical models with constant entrainment coefficients equal to the single-phase entrainment rate agree well with measurements of flow rates in multiphase plumes (Socolofsky, Bhaumik and Seol 2008). Hence, our concentration data confirm that net entrainment in a bubble plume can be modeled as a similar rate to single-phase plumes.

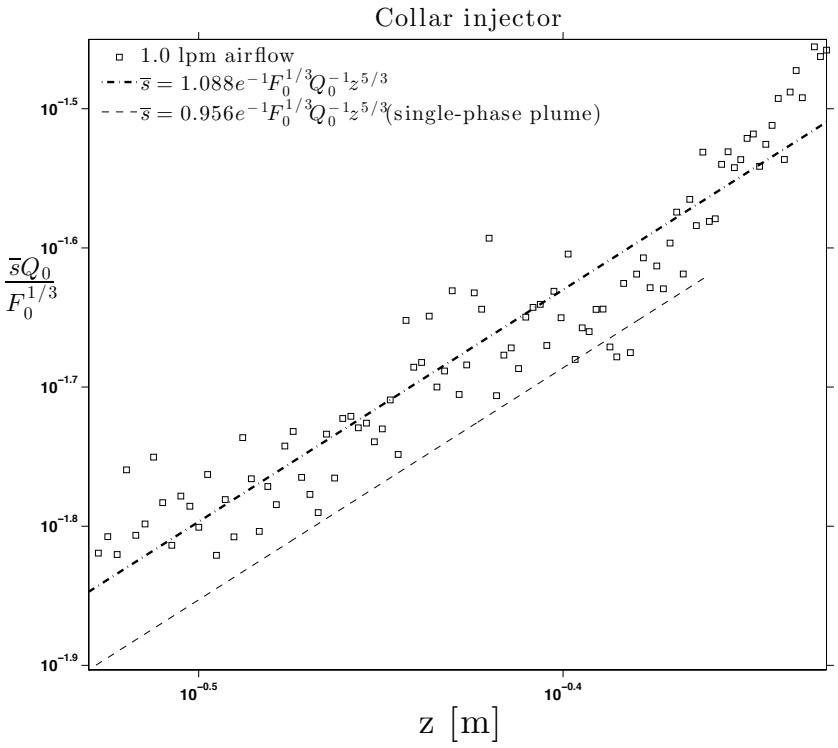

Figure 3-15 Centerline dilution

In Figure 3-16 and Figure 3-17, the time averaged and fluctuations of the concentration field are shown. Despite the asymmetry of the plume, the self-similarity property of the plume in both in-plane and out-of-plane direction is preserved for the normalized time averaged concentration field inside the bubble plume (Figure 3-16), where we normalize the x-axis and y-axis profiles using r/σ_x and r/σ_y, respectively.

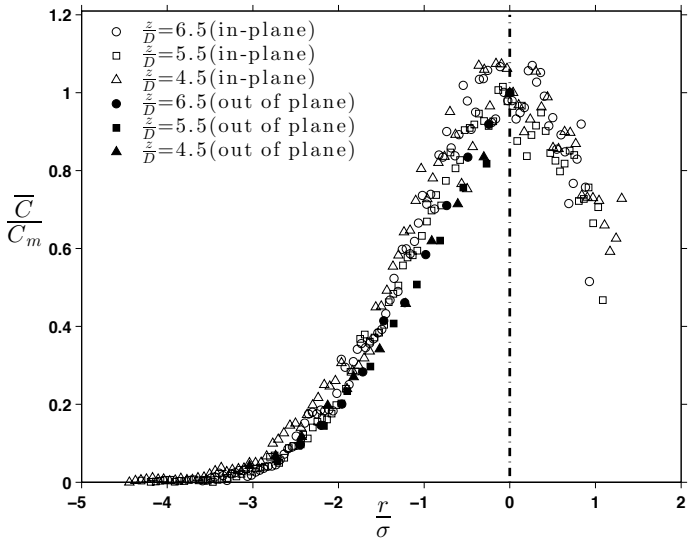

Figure 3-16 Time averaged concentration over the center-slice comparing to other slices on the centerline

Figure 3-17shows the normalized concentration fluctuation data with the x-axis scaled as in Figure 3-16. Maximum fluctuations levels are about 60% to 70% of the time-average value on the centerline, indicating a high level of concentration fluctuation. Based on the bubble detection data, the bubble core of the plume has a smaller radius comparing to the concentration field and the ratio in our experiments is $\frac{\sigma_b}{\sigma_y} = 0.8$, where σ_b and σ_y are the width of the bubble core and the concentration field respectively. The edge of the bubble core is shown as the dotted line in Figure 3-17, the fluctuations of the concentration field over this region is flatter than the Gaussian profile, which means that the presence of bubbles creates a homogeneously mixed concentration field inside of the bubble plume.

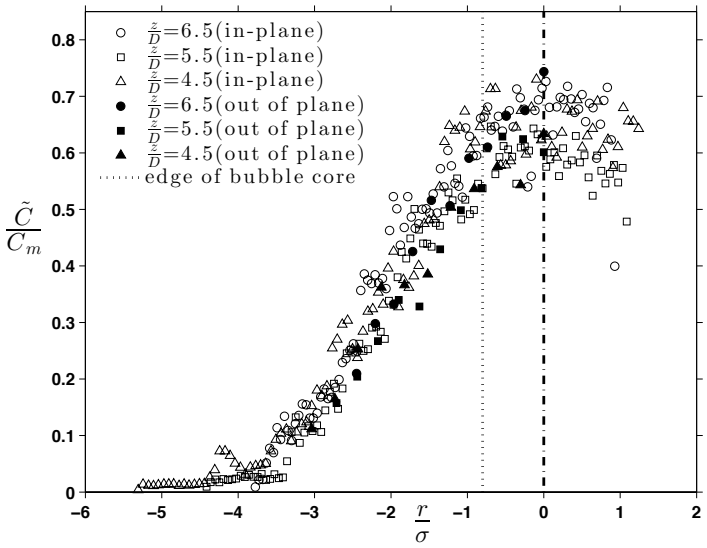

Figure 3-17 Concentration fluctuation over the center-slice comparing to other slices on the centerline

3.6 Conclusion

In this chapter, we developed and validated a measurement technique for the passive concentration field inside of a multi-phase flow. We adopted the 3D-PLIF technique to measure the concentration field inside of a bubble plume by considering the additional correction method to account for the presence of bubbles in the field of view. These additional corrections include removing bubble signatures from the recorded data and resolving intensity inhomogeneity due to the reflected light from surface of a bubble. Also, we introduced a new method to obtain a standard image from the recorded data by the experimental set-up. Following the proposed method, inherited uneven lighting signature as well as the vignette effects of camera lens are captured and are removed during the further correction process. We were able to validate our method by comparing the calculated concentration values from the obtained data with the actual concentration measurements

from the water sample inside of the experiment tank. The final results from this technique showed that the centerline dilution of a bubble plume is proportioned to $z^{\frac{5}{3}}$. The time averaged concentration field followed the self-similarity property of a plume. Concentration field has its maximum fluctuation around the centerline of the plume with values about 80% of the maximum concentration. It shows the centerline of the plume experience very low concentration values during the presence of the plume. Also, there is a broad region in the bubble core with uniform, high concentration fluctuation, indicating the strong mixing of the bubbles, yet, despite this mixing; non-uniformity of the initial dye injection is preserved to significant heights.

4 APPLICATION OF THE PLIF METHOD TO EVALUATE DISPERSANT INJECTION METHODS FOR SUBSEA CHEMICAL DISPERSANT INJECTION DURING ACCIDENTAL OIL WELL BLOWOUTS

4.1 Introduction

In the event of an accidental subsea oil well blowout, different mitigation methods, such as burning (Allen 1990, Allen and Ferek 1993)collecting and booming the surfaced oil (Fingas 2012, Morris 1983, Wong et al. 2005), and biodegradation of the oil (Atlas 1995, Bragg et al. 1994, Prince 1997), have been practiced to reduce the environmental impacts of the accident. Increasing the efficiency of these methods is the key goal for many research projects that suggested promptness in response to the accident as an important factor of improving the first two aforementioned mitigation methods to avoid weathering of the surface oil. For the cases that emphasize on the biodegradation of the oil, it is important to make the oil accessible to the bacteria by increasing the surface area per volume (A/V) of oil droplets. This can be achieved by breaking down big droplets into small droplets of oil, which is possible by reducing the interfacial tension between oil and water. One way to reduce the interfacial tension of the oil is by adding surfactants known as dispersant, into the leaked oil. In order to increase the process efficiency, the presence of a source of mixing energy like surface waves is necessary in the case of surface spray of the dispersant.

In the accident of the DeepWater Horizon, the dispersant was injected into the source of the blowout for the first time on a large scale. The goal was to use the mixing force of the rising turbulent plume of oil and gas to break up the oil into small droplets. At that time, a wand shaped injector was used to inject the dispersant into the source. It has been reported that 2.9

million liters of COREXIT 9500 was injected (Kujawinski, Kido Soule, Valentine, Boysen, Longnecker and Redmond 2011). The fate of the injected dispersant and dispersed oil was investigated by tracking the active ingredient of the COREXIT 9500, DOSS (Kujawinski, Kido Soule, Valentine, Boysen, Longnecker and Redmond 2011). It was shown that the correct understanding of the mixing process and the passive scalar concentration field inside the plume is the key element for studying the efficacy and effects of the new injection method.

In this section, we investigate the effects of the injection tool geometry on the created passive scalar concentration field inside a multi-phase plume. As an analogy to a blowout plume, we want to study the passive scalar concentration field inside a bubble plume as an example of multi-phase plumes. We created plumes with different airflow rates and injected a passive tracer dye into the plume through three different types of injectors: single point, wand, and a collar injector. Also, different injection heights were examined in the case of the single point injector. Results of this research will help to broaden our knowledge on the subject of the passive scalar concentration field inside multi-phase plumes. Additionally, the data can be used to specify the efficient injection procedure to be used in a case of future accidents.

The rest of this section is organized as follows. Part two presents the methodology of the experiments, consisting of test set-ups and scaling calculations. Then, we will discuss and explain the processed data from different experiment scenarios individually as well as thoroughly compare them in Part three. The last part of this section summarizes the conclusions derived from these experiments.

4.2 Methodology

4.2.1 Test set-up

We conducted our 3D Planar Laser Induced Fluorescence (3D-PLIF) experiments in a glass-wall tank that was 2 m long, 1.5 m wide, and 1.1 m tall in the Fluid Dynamics Laboratory of the Zachry Department of Civil Engineering at Texas A&M University. The water depth in the tank was kept constant at 0.95 m during all experiments, and purified water by reverse osmosis method was used to fill the tank. The plume source was a cylindrical air stone that was 14 mm in diameter and 20 mm in height. We placed the air stone on the bottom of the tank, with equal distance from the sidewalls and 0.50 m from the front glass wall. The tracer dye that we used in our experiments was a Rhodamine 6G dye that has a linear response to the laser light for concentrations below 50 μg/l (Ferrier, Funk and Roberts 1993) and its emission properties do not degrade due to light exposure (Crimaldi and Koseff 2001). The flow of the tracer dye was kept constant during each experiment by using a Mariotte bottle.

We used a high resolution CCD camera (Flow Master 3S, 12 bit intensity depth with 1024x1280 pixel resolution) to record the fine details of the flow structure and concentration field. The camera was directly connected to a high-speed hard drive to save the recorded frames on-line; therefore, the duration of the experiments was not a limit from the recording device. A 5-Watt continuous wave Nd-Yag solid-state laser (Spectra-Physics Millennia Edge Single Frequency CW) was the light source for our experiments. It had reliable output power, with less than 5% fluctuations in the course of an experiment and that was monitored by a Coherent FieldMaxII-TOP power-meter. The 3D illumination of the field of view was created by means of a scanning mirror (Model 6220MH60, Cambridge Technology, Inc.) mounted on a motorized linear stage (A-LST0750B Zaber technologies Inc.). With this set-

up, the laser sheet was kept perpendicular to the camera axis; therefore, there was no need to use Plano-convex lenses (Tian and Roberts 2003).

The camera, scanning mirror, and the linear stage used in our experiments were synchronized in Lab-VIEW.

4.2.2 Scaling

To compare our results to the field scale, we considered the dynamic similitude of the bubble plume flow. The scaling length scale we used in our calculations was the bubble plume length scale, D, introduced by Bombardelli, Buscaglia, Rehmann, Rincón and García (2007). The bubble plume length scale is a new representation of the balance between inertia and buoyancy. The bubble plume length scale, D, is formulated as:

$$D = \frac{gQ_g(0)}{4\pi\alpha^2 w_b^3} \tag{4-1}$$

Where, $Q_g(0)$ is the initial gas flow rate, α is the entrainment coefficient (taken as 0.083), and w_b is the bubble slip velocity. This length scale divides the plume into three regions. The first region is $z \le 10d_0$, where d_0 is the diffuser diameter. In this region the behavior of the plume is directly influenced by its initial conditions. As the plume reaches the edge of this region, the densimetric Froude number approaches 1.7, its asymptotic value for the centerline of open source plumes (Wüest, Brooks and Imboden 1992). Distances in the range of $10d_0$ to 5D are called the intermediate region. In this region, the plume behavior has not reached the asymptotic solution, but it is not under the strong influence of initial conditions either. Most environmental applications of multi-phase plumes are in this region, as are the majority of

the laboratory and field data. The last region is the asymptotic region where the plume is reached the asymptotic solution and its behavior no longer depends on its initial condition. This region begins at $z \cong 5D$ from the plume source.

The values of bubble length scale for our plume and the Deep Water Horizon (DWH) accident are reported in Table 4-1.

Table 4-1 Bubble plume length scale for the lab tests

Test No.	Injector type	Injection position	D [m]			l_b [m]		
			0.5 [l/min]	1.0 [l/min]	1.5 [l/min]	0.5 [l/min]	1.0 [l/min]	1.5 [l/min]
1	Collar	y=0, z=20 mm						
2	Wand	y=0, z=20 mm						
3	Single point	y=-d/2*, z=20 mm	0.035	0.070	0.105	0.7	0.56	0.48
4		y=-l_M†, z=20 mm						
5		y=-l_M, z=5.2d						

* d is the diameter of the air stone

†l_M is the momentum length of the tracer dye effluent

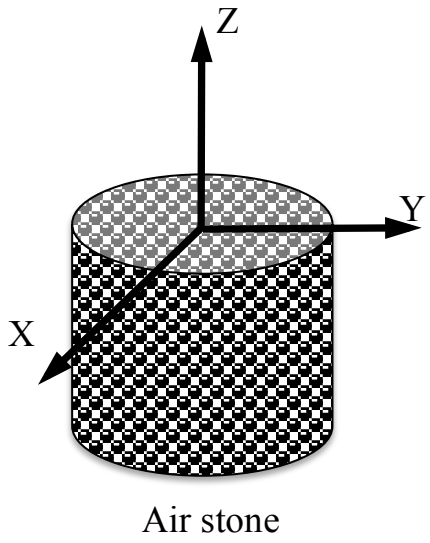

Figure 4-1 Coordinate system of the laboratory test

During the DWH, there were three main types of releases. Initially, all of the flow exited the end of the broken riser on the sea floor (case 1). After some time, a second source appeared at the kink in the riser directly above the blowout preventer (case 2). During that period, flow exited both the kink and the broken riser. For a short period after the blowout preventer was removed and before the top hat was installed, oil exited directly from the top of the wellhead (case 3). The flow rate for each of these sources is slightly different, hence, each release had a different characteristics scale. Table 4-2shows an estimate of the average discharge conditions and the parameter D for each of these cases. In our experiments, the base of the imaging plane was a fixed height z = 0.295 m above the bubble plume diffuser. The final three columns in Table 4-2 report the physical height during the Deepwater Horizon that our measurement plane represents above the actual discharge using z/D as the scale parameter. From the Table, we see that our measurement plane is well above the source, even beyond the free surface, for the cases where the full discharge is exiting the riser. For the kink flow

rate, our measurement plane is similar to the height of the intrusion layer. This is a common problem with scale analysis between field and laboratory experiments. In order to have an effective measurement plane near the Deepwater Horizon source, we would have to measure very near the diffuser, where the void fraction makes measurements difficult to impossible. Hence, our measurements represent the mixing that is achieved very far away from the injection--which is similar to the maximum amount of mixing possible between the discharge and the injected dispersant.

To compare results between experiments, we used another key scaling parameter, the buoyancy length scale given by:

$$l_b = \frac{F_0}{u_c^3} \tag{4-2}$$

where, F_0 is the initial buoyancy flux of the plume and u_c is the plume velocity at the source (see values reported in Table 4-1). We did not measure u_c in our experiments. To compute l_b, we used an integral model for bubble plumes to predict the value of u_c at our measurement plane for each experiment. The model was that in Socolofsky, Bhaumik and Seol (2008). Based on these values for u_c for the three flow rates used in our experiments, the non-dimensional height $z/l_b = 0.65$ occurred within the measurement plane for each experiment. Hence, when plotting data for different experiments, we extract the results at $z/l_b = 0.65$ to have dynamic similitude among the results. The values of z/D at these heights are 13, 5.2, and 2.97 for the flow rates of 0.5, 1.0, and 1.5 l/min, respectively. Therefore, we are not comparing results at the same bubble plume length scales but rather at characteristic scales of the buoyancy.

Table 4-2 Bubble plume length scales for the DWH

Case	D [m]	z [m] (based on z/D)		
		0.5 [l/min]	1 [l/min]	1.5 [/min]
Case 1	2145.28	3006.179	1503.09	1002.06
Case 2	310.18	434.65	217.325	144.883
Case 3	2210.01	3096.88	1548.44	1032.3

4.3 Results and discussion

To study the efficiency of different injector types that are possible to be used in the subsea injection process of dispersant, we used three injectors: collar, wand, and single point injectors. The collar and wand injectors were fabricated in a way that the injected fluid through their orifices with the specified injection rate does not have a significant amount of momentum and the reason was eliminating of any disturbance to the flow structure created by the bubble plume. In the case of the single point injector, it was not possible to eliminate the effluent momentum due to its shape. Instead, we examined different injection points for this injector to study the effects of momentum on the created concentration field. We moved the single point injector back a momentum length from the edge of the air diffuser and in the other scenario it was elevated to the height corresponding to the zone of flow establishment (ZFE). Each injector type was examined for three flow-rates of bubble plume.

We used the following coordinate system to synthesize our data. Each camera image is in a plane with z positive upward and y as the horizontal coordinate. These yz-image planes were in line with the laser light sheet, which scanned from top to bottom and in reverse along the

y-axis. As the experiments progressed, the linear stage moved the light sheet toward and away from the camera along the x-axis (normal to the image plane). The position (0,0,0) is taken at the top of the diffuser. For the time averaged and concentration fluctuations profile graphs presented here, we analyzed a subset of the data. We linearly chose 100 out of 1024 points along the y-axis in the field of view. In the case of concentration dilution along the vertical axis, 50 data points were chosen to represent the behavior of the concentration field rising in the plume.

4.3.1 Collar injector

The collar injector has holes on its inner surface that inject effluent toward the core of the plume (Figure 4-2); note that the dye does not exit the black T connector shown in the image. In our experiments, the collar injector had a 30 mm inner diameter and was placed 20 mm above the air diffuser. The 3D reconstruction of the time averaged passive concentration field created by the collar diffuser is shown in Figure 4-3. It should be mentioned that due to the non-uniform spacing of the holes on the collar injector, the created concentration field has not equal spreading radius in x and y direction and because there was no swirl motion in the bubble plume velocity field, the non-uniform initial condition of the dye source was preserved all the way to the water surface.

Figure 4-2 Collar injector installation configuration

The time averaged concentration field ($\bar{C}$) is created by averaging 300 images, 2.5 s apart from each other. We also computed the standard deviation of concentration fluctuations (C_{rms}). A profile of $\bar{C}$ and C_{rms} at z=0.36 m is shown in Figure 4-4.

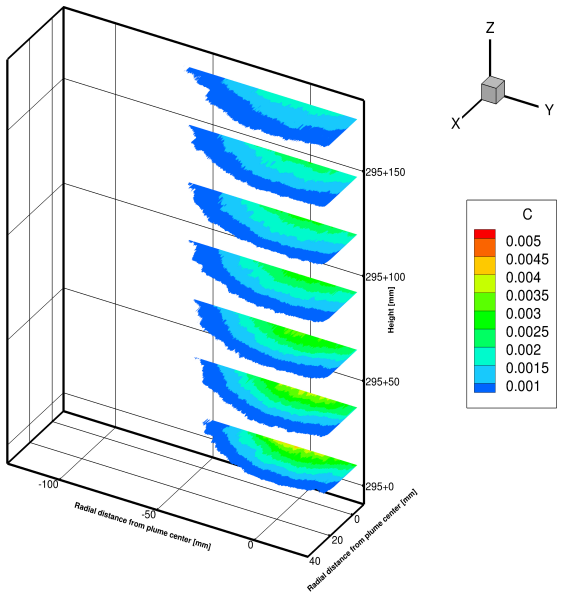

Figure 4-3 3D construction of time averaged concentration field - collar injector mg/l

From the figure, we can conclude that the time averaged concentration field normalized by the centerline concentration value (C_m) has a normal distribution and that the center of the tracer data coincides with the air diffuser (dashed line).

Increasing the flow rate caused the amount of maximum fluctuation to be reduced, creating a more steady presence of the tracer dye concentration in the flow field (Figure 4-4(b)). The light dotted line in Figure 4-4(b) gives the edge of the region occupied by bubbles. It can be seen from Figure 4-4(b) that the slope and magnitude of the fluctuation profile is reduced by the increase in the airflow rate. The amount of fluctuations in the case of 1.0 l/min flow rate is constant over the core of the bubble plume. This demonstrates a uniform mixing in the bubble core region.

Figure 4-5 shows the growth rate of the plume in the y-direction, given by standard deviation of the time-averaged concentration in a non-dimensional form. The radius and height were normalized by the bubble plume length scale.

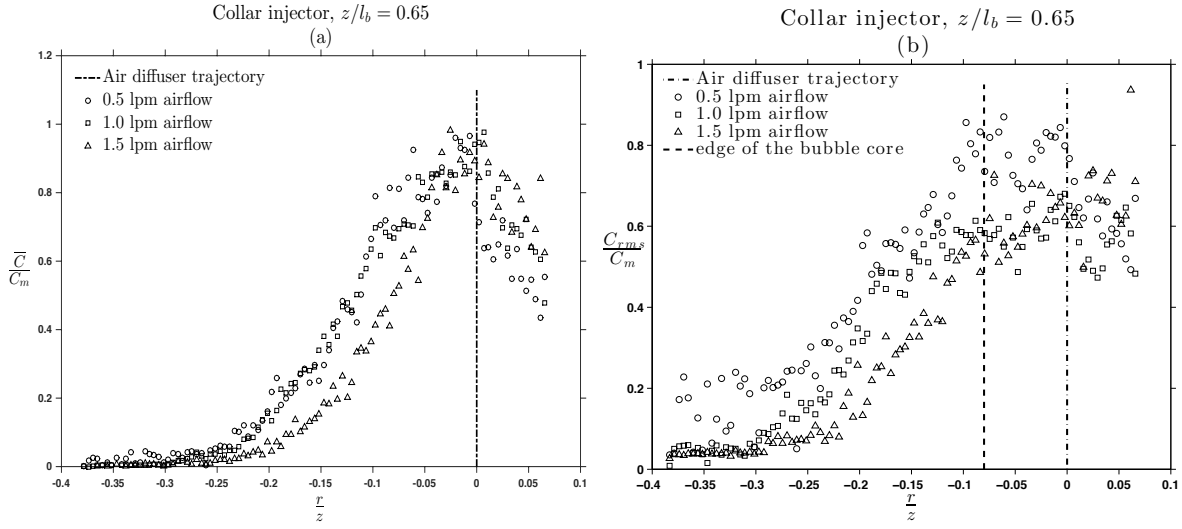

Figure 4-4 Time averaged (a) and rms of fluctuation (b) for collar injector

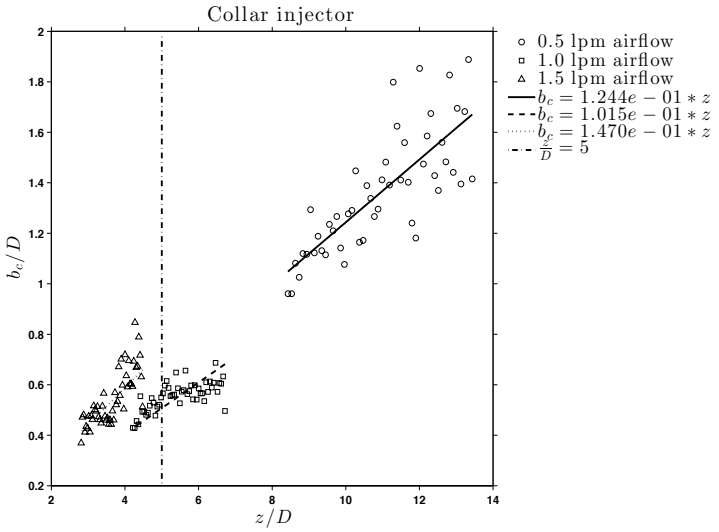

Figure 4-5 Plume half-width defined by concentration (b_c) - collar injector

The other parameter of the measured concentration field is the concentration dilution (Figure 4-6). For the single-phase plume, Lee and Chu (2012) calculated that the centerline dilution of the plume is proportional to $z^{5/3}$ based on Eq.(4-3).

$$\frac{\overline{s}Q_p(0)}{F_0^{1/3}} = 0.096 \cdot z^{5/3} \tag{4-3}$$

Where $Q_p(0)$ is the initial flow rate of the plume, and F_0 is the initial buoyancy flux of the plume:

$$F_0 = \left(\frac{\rho_a - \rho_b}{\rho_a} \right) g Q_o \tag{4-4}$$

Where ρ_a and ρ_b are ambient and bubble density, respectively, and Q_0 is the initial gas flow rate of the plume.

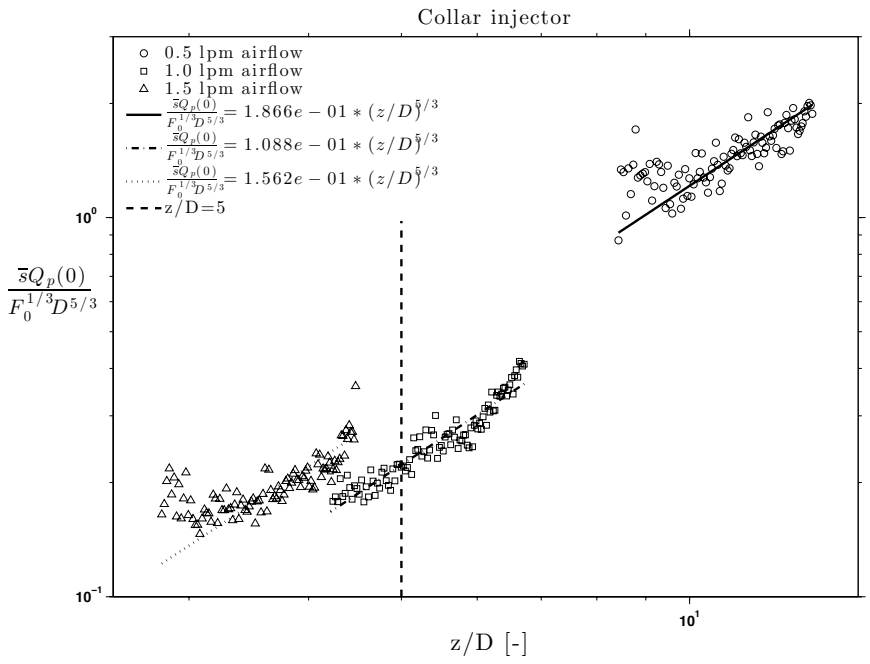

Figure 4-6 Concentration dilution along the plume centerline (collar injector)

In Eq.(4-3), $Q_p(0)$ is the plume initial flow rate, which in the case of a bubble plume, is created by the entrained ambient fluid in the plume. To calculate the plume flow generated by the airflow in the ambient, we used the work of Wüest, Brooks and Imboden (1992). In their paper, they explained that the densimetric Froude number for the centerline of the bubble plume reaches the asymptotic value of 1.6 at the end of the ZFE. They defined the densimetric Froude number as:

$$Fr = \frac{w}{\sqrt{2\lambda b\left(\rho_a - \rho_p\right)/\rho_p}} \tag{4-5}$$

Where w is the plume raise velocity, λb is the radius of top hat bubble core velocity, and ρ_a and ρ_p are the ambient and plume density, respectively. The plume density is defined as:

$$\rho_p = \left(1 - V_g\right)\rho_w \tag{4-6}$$

Where V_g is the volumetric void fraction inside the plume. By iterative calculation, we could calculate the plume flow rate at the end of the ZFE (Socolofsky and Bhaumik 2008). We used the same number as the initial plume flow rate for further calculations. We normalized the centerline dilution of our data based on the left-hand side of Eq. (4-3). In Figure 4-6, we did not nondimensionalize the distance, as a result the data was not collapsed into one graph. The concentration dilution rate in our experiments is within a factor of 2 to the dilution rate of the single-phase plume reported by Lee and Chu (2003).

4.3.2 Single point injector (1st position)

The Single point injector was simply made out of a 1/8 in tube. In the first position, the end of the pipe was flushed with the edge of the air diffuser at a height of 20 mm above the air stone (Figure 4-7).

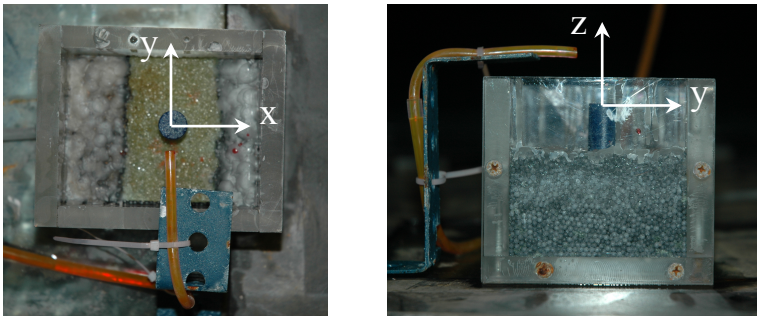

Figure 4-7 Single point injector installation configuration

In the case of the single point injector, we observed a significant amount of effluent momentum that could not be disregarded. With a 3.41 ml/s injection rate, the momentum length scale of the tracer dye effluent was 0.12 m.

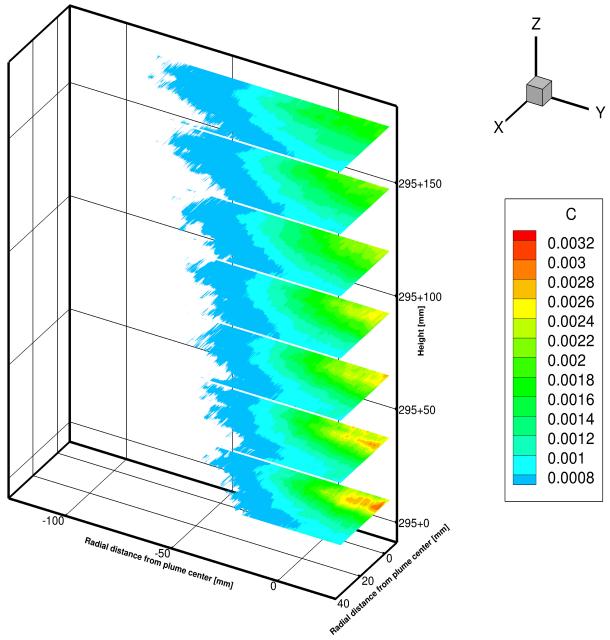

Figure 4-8 3D construction of time averaged concentration field - single point injector 1st position mg/l

The effluent momentum caused a shift in the center of the concentration field toward the opposite side of the plume. As a result, the centerline of the time averaged concentration field was pushed toward the opposite edge of the field of view (Figure 4-9(a)). As the gas flow rate in the bubble plume increased, stronger ambient water entrainment into the plume overcame the strength of the momentum jet and reduced the amount of shift in the concentration field. Comparing the profiles of 0.5 and 1.5 l/min bubble plume clarifies the amount of shift in the case of 0.5 l/min flow rate and that the center of the concentration field was outside of the field of view. This means that some of the injected tracer dye solution is pushed out from the opposite side of the plume, and it did not uniformly cover the plume

core. But in the case of a more energetic plume (1.5 l/min), the concentration field is more symmetric around the centerline of the bubble plume.

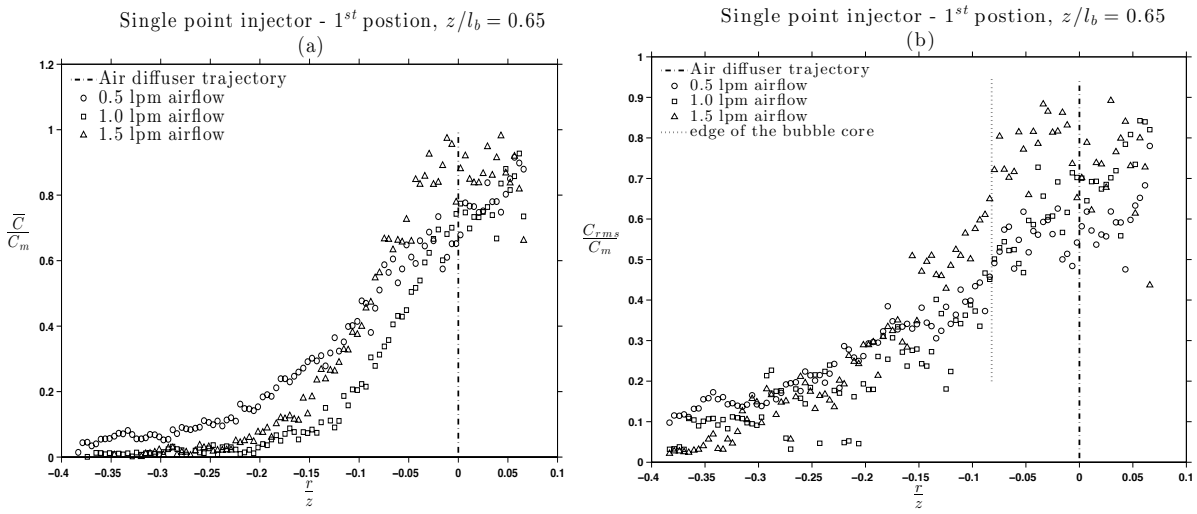

Figure 4-9 Time averaged (a) and rms of fluctuation (b) for single point injector 1st position

The concentration fluctuation in the case of the single point injector spreads out of the core of the bubble plume and covers a bigger area. The fluctuations have the same order of magnitude as the centerline concentration, which indicates a very intermittent concentration field.

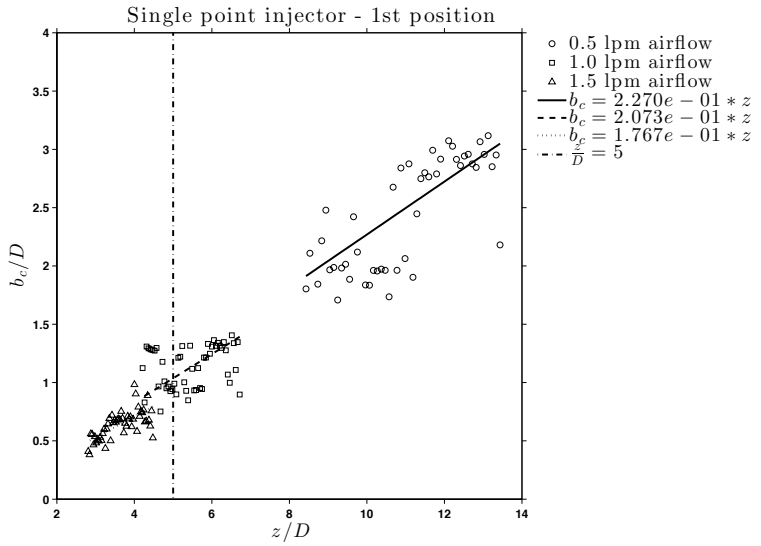

Figure 4-10 Plume half-width defined by concentration (b_c) – single point injector 1st position

Comparing the half-width of the concentration field, we can see the increase in the gas flow rate of the plume did not have a significant effect on the growth rate of the concentration field (Figure 4-10).

4.3.3 Single point injector (2nd position)

In order to remove the effect of the tracer dye effluent momentum from the experiment, we moved the tip of the single point injector back a momentum length from the edge of the air diffuser, which was 0.12 m (Figure 4-12). Figure 4-13 presents the time averaged dye distribution.

It can be seen from Figure 4-14(a) that the centerline of the concentration field moved back inside the plume core with a slight shift toward the right side of the field of view.

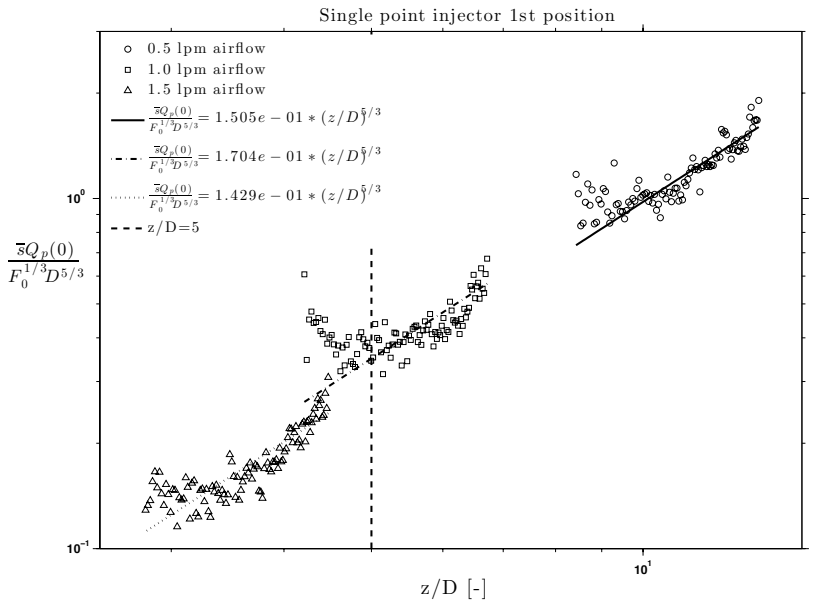

Figure 4-11 Concentration dilution along the plume centerline (single point injector 1st position)

The time-averaged concentration profile does not show any irregular behavior, but the concentration fluctuation profile indicates fluctuations as large as the centerline concentration value. It shows that the single point injector is not capable of creating a stable concentration field even when the momentum of the effluent jet is damped before reaching the bubble plume. As for the previous injection position, the growth rate of the concentration field was not affected by the flow rate of the bubble plume.

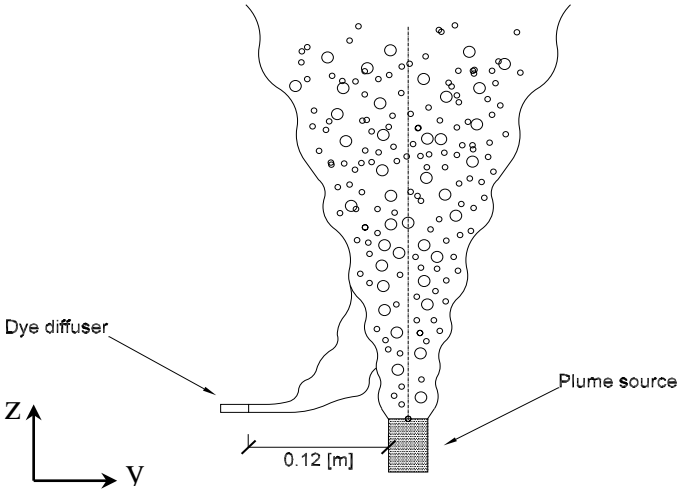

Figure 4-12 Single point injector – 2nd position

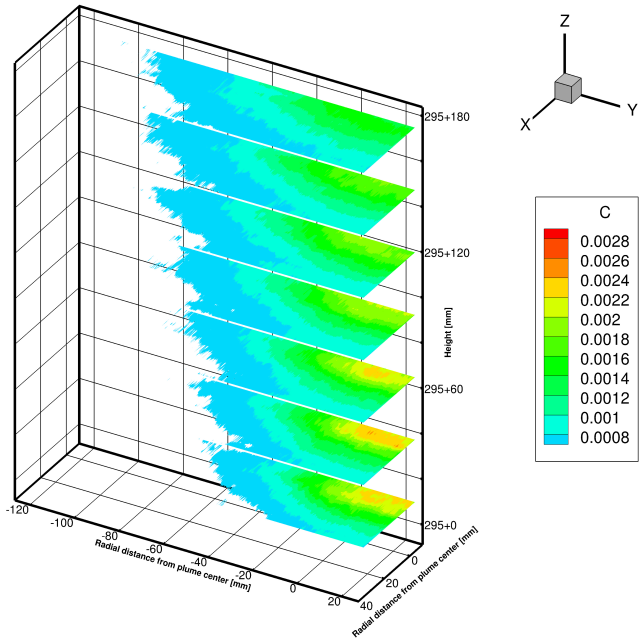

Figure 4-13 3D construction of time averaged concentration field - single point injector 2nd position mg/l

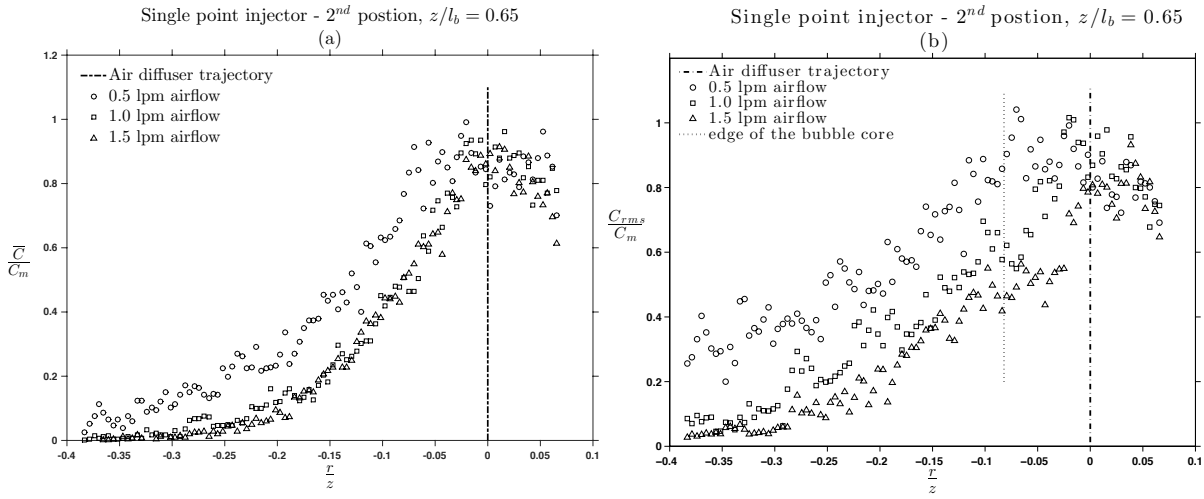

Figure 4-14 Time averaged (a) and rms of fluctuation (b) for single point injector 2nd position

The centerline dilution of the concentration field for different flow cases is improved by increasing the airflow rate in the plume.

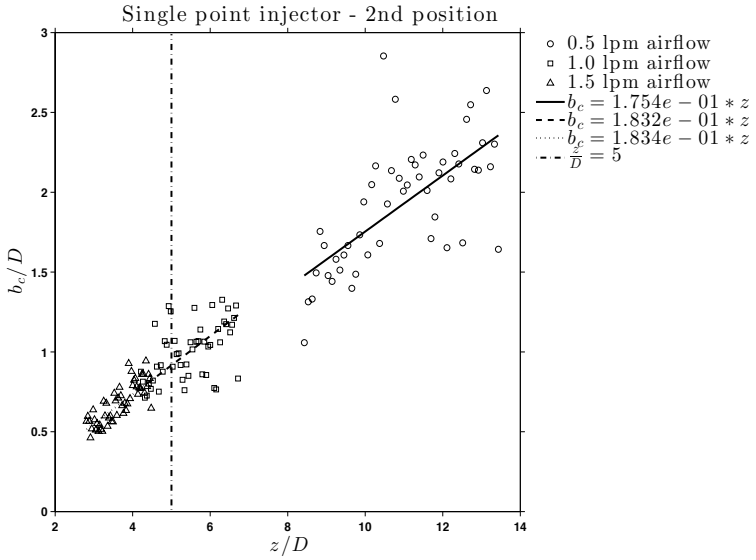

Figure 4-15 Plume half-width defined by concentration (b_c) – single point injector 2nd position

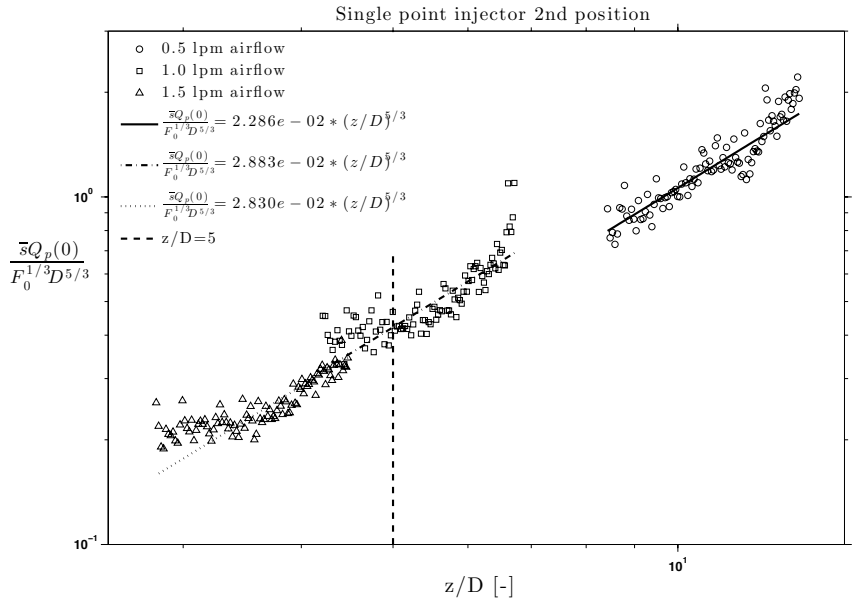

Figure 4-16 Concentration dilution along the plume centerline (single point injector 2nd position)

4.3.4 Single point injector (3rd position)

One of the scenarios we wanted to examine was the effect of injection elevation on the passive scalar concentration field. To create this condition, we raised the position of the single point diffuser to the end of the ZFE. For plume type flow structures, the height of ZFE is $5.2d_0$ (Lee and Chu 2012), where d_0 is the diameter of the plume source. In our experiments, we used a 14 mm air stone as a source of the plume; as a result, the height of the ZFE in our experiment was about 73 mm. A schematic sketch of the set-up is shown in Figure 4-17.

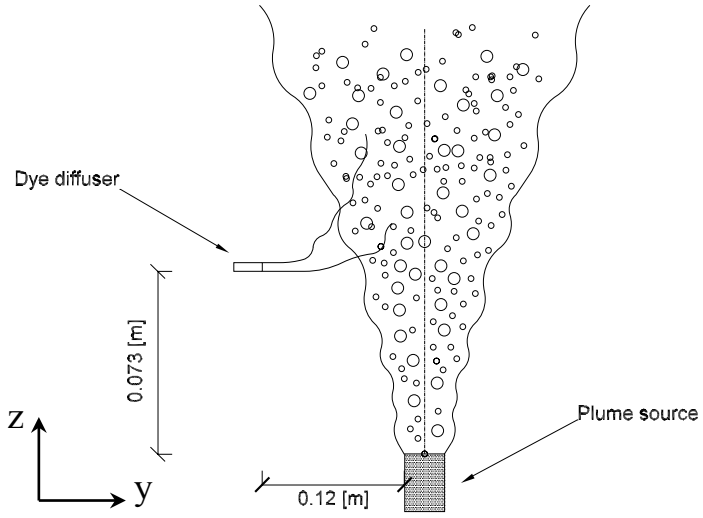

Figure 4-17 Single point injector – 3rd position

The generated concentration field is comparably narrower than previous cases of the single point injector (Figure 4-19(a)). Since the injection point was closer to the field of view, the concentration field had less opportunity to diffuse and spread. High fluctuating levels of concentration, on other hand, were extended far beyond the half-width of the concentration field (Figure 4-19(b)). And, the magnitude of the fluctuation was in the order of the centerline concentration values. The other noticeable difference here is the lack of improvement of centerline dilution by increasing the airflow rate (Figure 4-21). The reason is that, due to relatively closer distance of the field of view to the point of injection, the injected tracer dye did not have enough time to mix thoroughly in the plume; hence, the amount of available mixing due to the higher airflow rate became an important parameter (Figure 4-21).

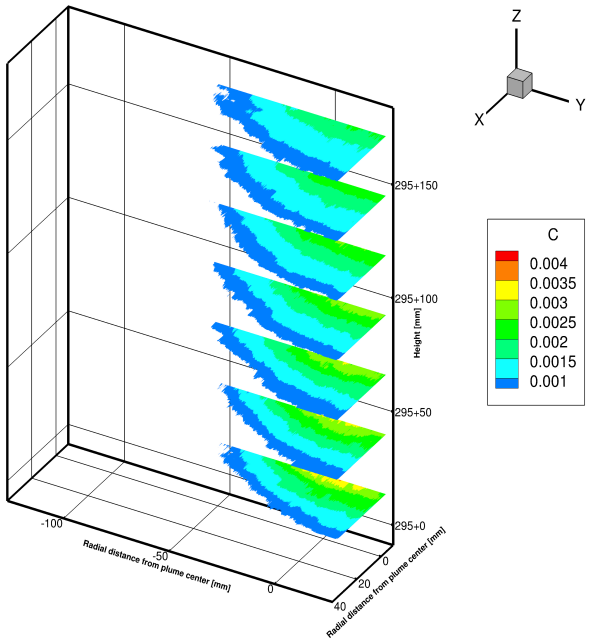

Figure 4-18 3D construction of time averaged concentration field - single point injector 3rd position mg/l

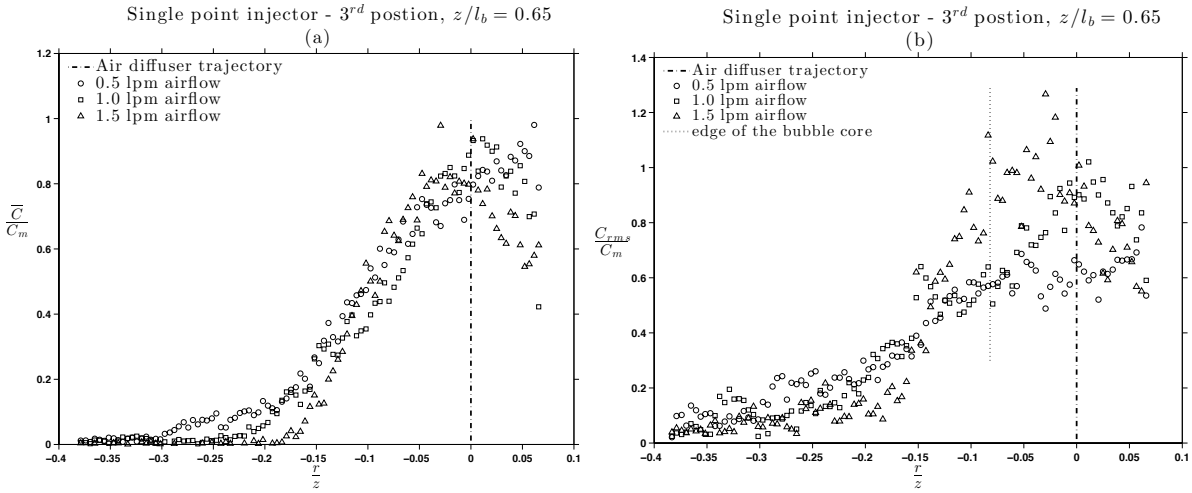

Figure 4-19 Time averaged (a) and rms of fluctuation (b) for single point injector 3nd position

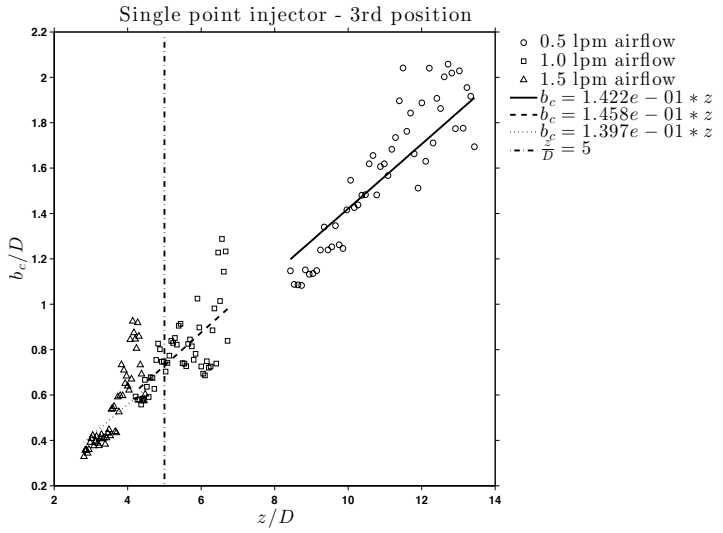

Figure 4-20 Plume half-width defined by concentration (b_c) – single point injector 3rd position

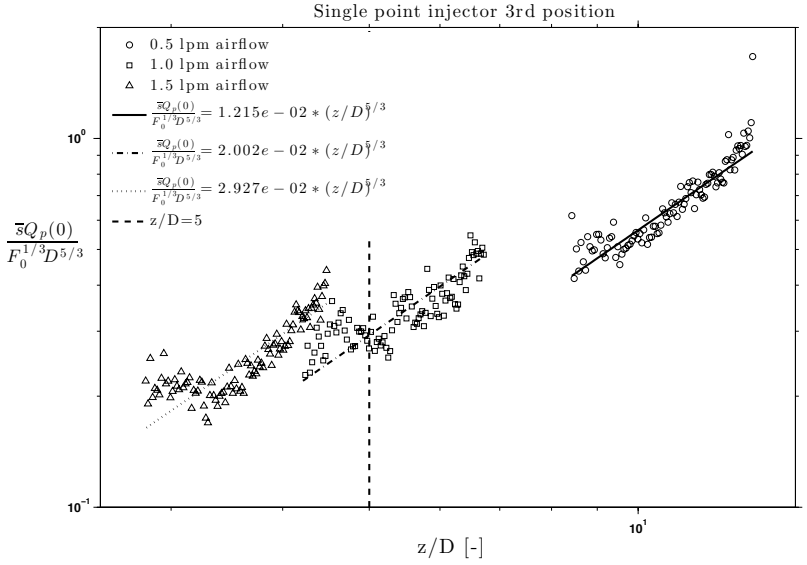

Figure 4-21 Concentration dilution along the plume centerline (single point injector 3rd position)

4.3.5 Wand injector

The wand injector was a straight pipe that consisted of orifices over the length of 0.03 m (Figure 4-22). It was placed above the air diffuser at a height of 20 mm, and its orifices faced upward. The 3D reproduction of its concentration field is shown in Figure 4-23.

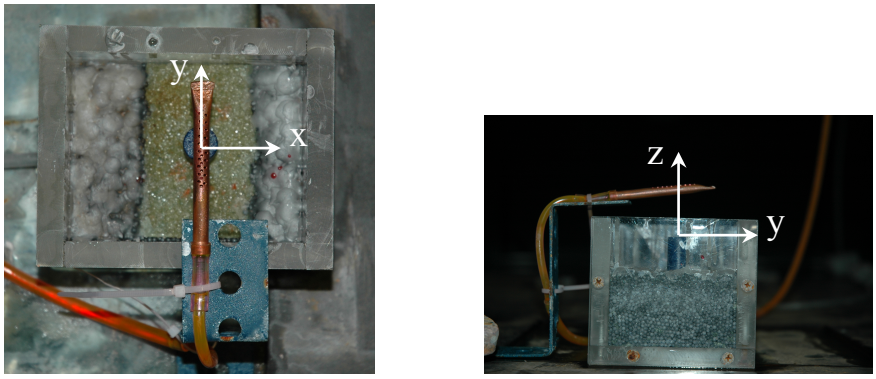

Figure 4-22 Wand injector installation configuration

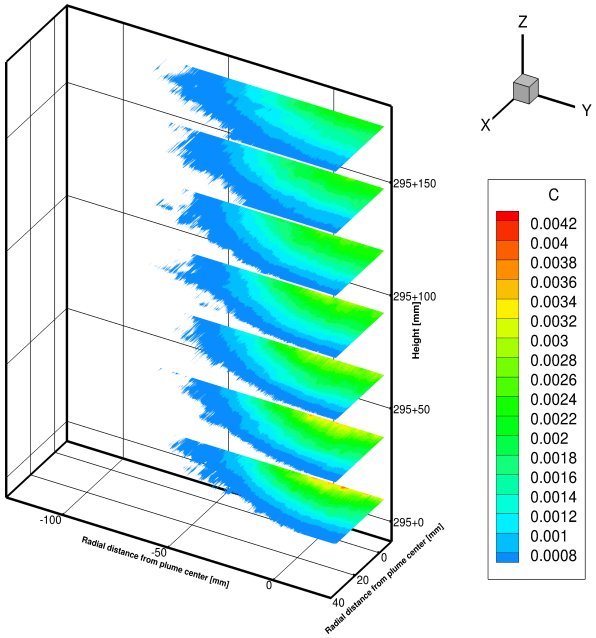

Figure 4-23 3D construction of time averaged concentration field - wand injector mg/l

The concentration field generated by the wand injector in the x=0 plane is symmetric around the centerline of the plume and is normally distributed (Figure 4-24(a)). As the airflow rate of the plume was increased, the half-width of the concentration field was broadened as a result. The fluctuation of the concentration field is isolated around the plume centerline for 1.0 l/min profile. For the higher flow rate profiles, the concentration fluctuation spreads out and covered most of the plume width (Figure 4-24(b)). At the same time, the magnitude of fluctuations was reduced to 80% of the mean concentration value. The centerline dilution of the concentration field generated by the wand injector had the same trajectory as $z^{5/3}$ and it was improved by the additional amount of turbulent mixing energy added due to the increase of the airflow rate of the plume (Figure 4-26).

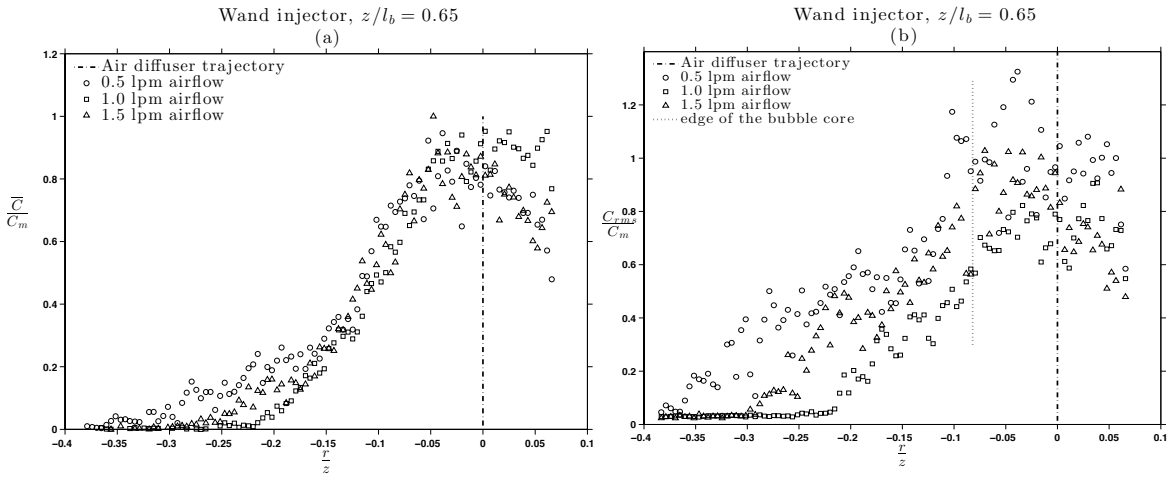

Figure 4-24 Time averaged (a) and rms of fluctuation (b) for wand injector

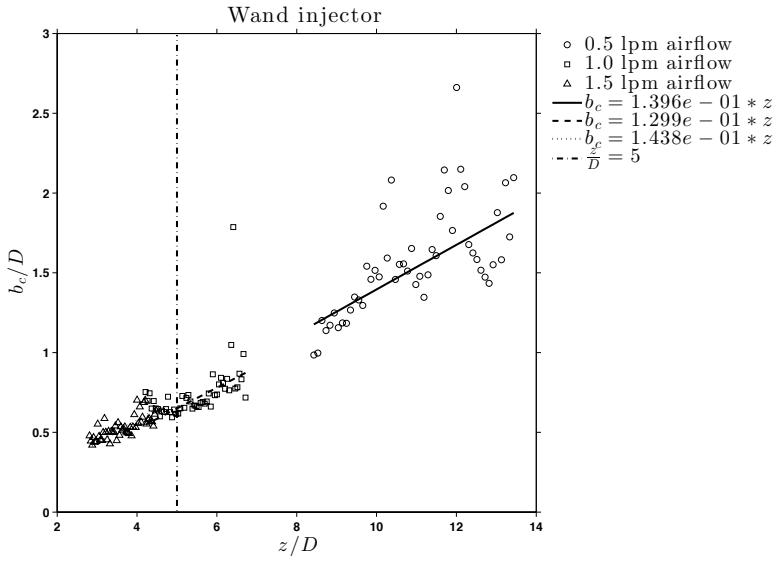

Figure 4-25 Plume half-width defined by concentration (b_c) - Wand injector

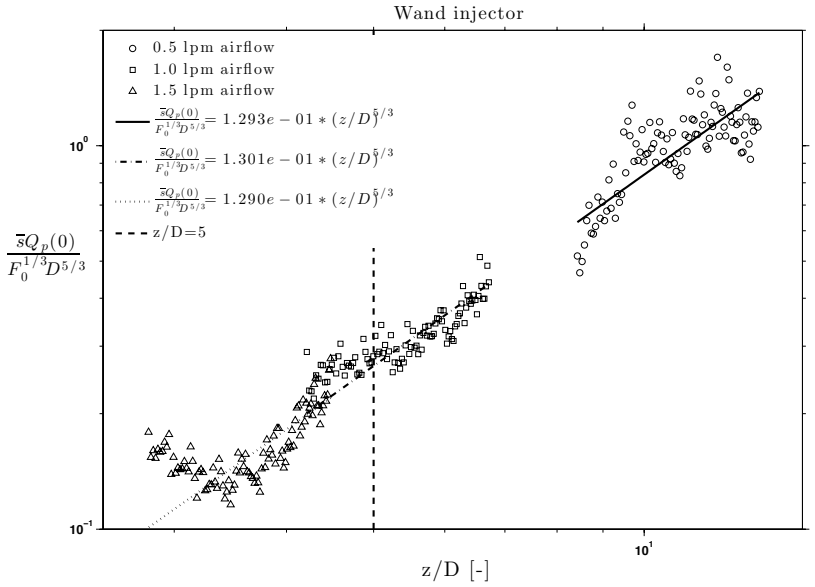

Figure 4-26 Concentration dilution along the plume centerline (wand injector)

4.3.6 Comparing different injectors

By extracting the physical characteristics of the concentration field created by each of the injectors, we are able to compare their performance. Figure 4-27 plots the normalized averaged concentration and concentration fluctuations for different injectors for the 1.0 l/min airflow rate. The data in the figure is plotted in away that the centerline of the bubble core for different data points are aligned; therefore, the data points for the single point injector on its first position were shifted to the right. Figure 4-27(a) shows the comparison of the normalized time-averaged concentration profile due to different injectors for the 1.0 l/min airflow rate and at the height equal to $0.65l_b$. It can be seen that the area of the plume that was covered by the concentration field created by the collar injector is wider comparing to the single point injector on its first position, where the concentration field was pushed outside of the plume core. This means that using the single point injector close to the edge of the plume can reduce the efficiency of the injection process. Figure 4-27(b) shows that for the collar injector, the maximum amount of fluctuation is limited to 60% of the centerline concentration, and it is constant over the width of the plume. Also, it can be seen that for the collar and wand injector the extent of concentration fluctuation is limited to the borders of the concentration field (r/z=-0.2) when compared to the single point injector.

Figure 4-28 compares the plume half-width by concentration for different injectors.

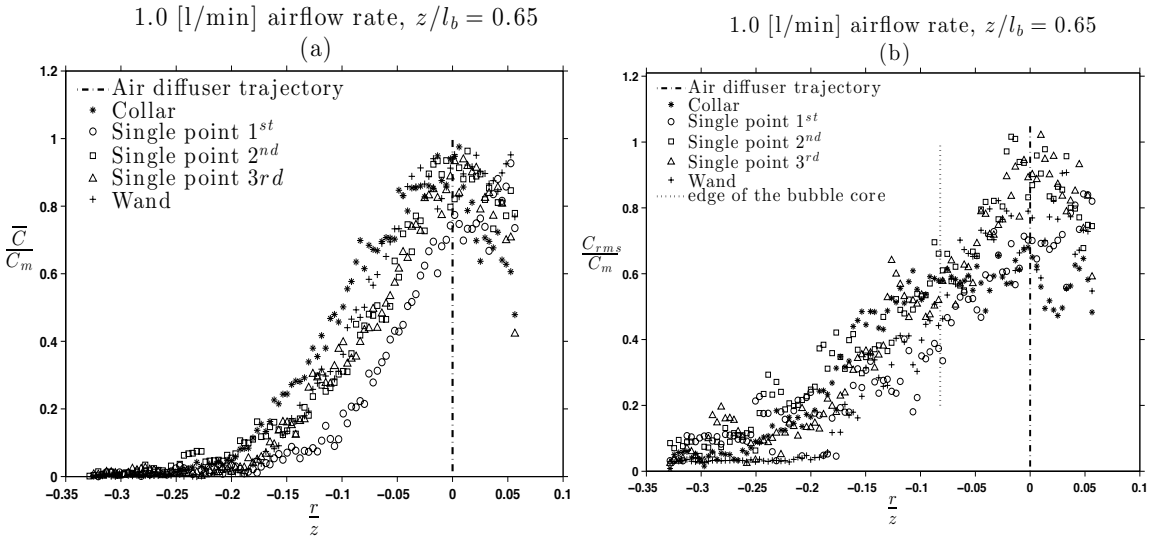

Figure 4-27 Time averaged (a) and rms of fluctuation (b) for 1.0 l/min airflow rate

Based on Figure 4-28, the concentration fields generated by the collar and wand injectors had a slower growth rate when compared to the single point injector for its different injection positions. Because the collar and wand injectors inject the tracer dye inside the plume core, it is less likely that the dye spreads outside of the plume core. Whilst the injected dye through the single point injector at the edge of the air-stone or a momentum length away of the plume source mixed with the rising water in the vicinity of the plume and can spread wider than plume half-width.

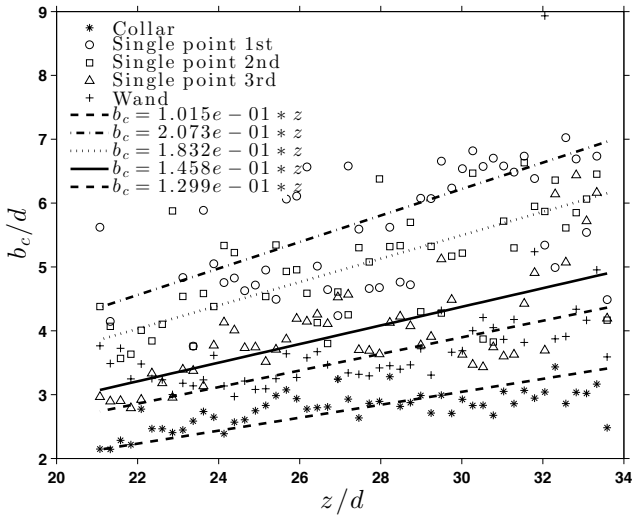

Figure 4-28 Plume half-width by concentration - 1.0 l/min

Table 4-3 is the list of the plume half-width calculated based on the concentration field. To calculate these values, the Gaussian profile was fitted to the data and the spread value of the profile was assumed as the half-width of the plume. One trait that all of the injector types follow is that the increase in the airflow rate of the plume, confines the spread rate of the concentration fields. Also, all of the concentration fields have a larger spread rates in the y-direction than the x-direction. For the collar injector, we mentioned that the uneven spacing between the openings of the injector caused the asymmetric concentration field. For the wand injector, the shape of the injector dictated the larger spread in the y-direction comparing to the x-direction, and injecting of the dye into the plume in the y-direction in the case of single point injector was the reason for wider spread of its concentration field in y-direction.

Table 4-3 Half-width of the plume based on concentration field at z/l_b=0.65

Test No.	Injector type	σ_y [m] (at z/l_b = 0.65)			σ_x [m] (at z/l_b = 0.65)			σ_y/σ_x		
		0.5 [l/min]	1.0 [l/min]	1.5 [l/min]	0.5 [l/min]	1.0 [l/min]	1.5 [l/min]	0.5 [l/min]	1.0 [l/min]	1.5 [l/min]
1	Collar	0.058	0.04	0.035	0.032	0.027	0.025	1.81	1.48	1.40
2	Wand	0.062	0.045	0.039	0.041	0.037	0.033	1.51	1.22	1.18
3	Single point 1st position	0.097	0.071	0.061	0.062	0.041	0.035	1.56	1.73	1.74
4	Single point 2nd position	0.082	0.07	0.052	0.051	0.042	0.029	1.61	1.67	1.79
5	Single point 3rd position	0.065	0.059	0.048	0.049	0.040	0.035	1.33	1.47	1.37

The other factor for checking the efficiency of different types of injectors is their centerline dilution. Figure 4-29 shows the trajectory of centerline dilution versus the height of the plume. The definition of dilution is the ratio of initial concentration to the maximum concentration at any height:

$$\overline{s} = \frac{C_0}{C_m} \tag{4-7}$$

In the case of collar injector, wand injector and single point injector on its first position, the initial concentration used in this equation was the tracer dye solution concentration, since the tracer dye was injected directly into the plume. For the single point injector on its second and third position experiments, the outlet of the injection pipe was away from the plume, so the concentration of the tracer solution was diluted before it reached the bubble plume. I calculated the maximum concentration of the effluent at the time of reaching the plume

centerline by following Lee and Chu (2012) formula for measuring the centerline concentration in the case of single-phase jet as:

$$\frac{C_m}{C_0} = 5.26\left(\frac{x}{d}\right)^{-1} \tag{4-8}$$

Where d is the source diameter, x is the distance from the source and C_0 and C_m are the initial and centerline concentration, respectively. In our experiments, the initial concentration of tracer dye solution was 0.65 mg/l and the distance x from the injection point to the edge of the plume was 0.12 m and the injector diameter, d, was 3.175 mm. Using these numbers, the centerline concentration of the tracer dye jet at the edge of the plume was calculated as 0.091 mg/l.

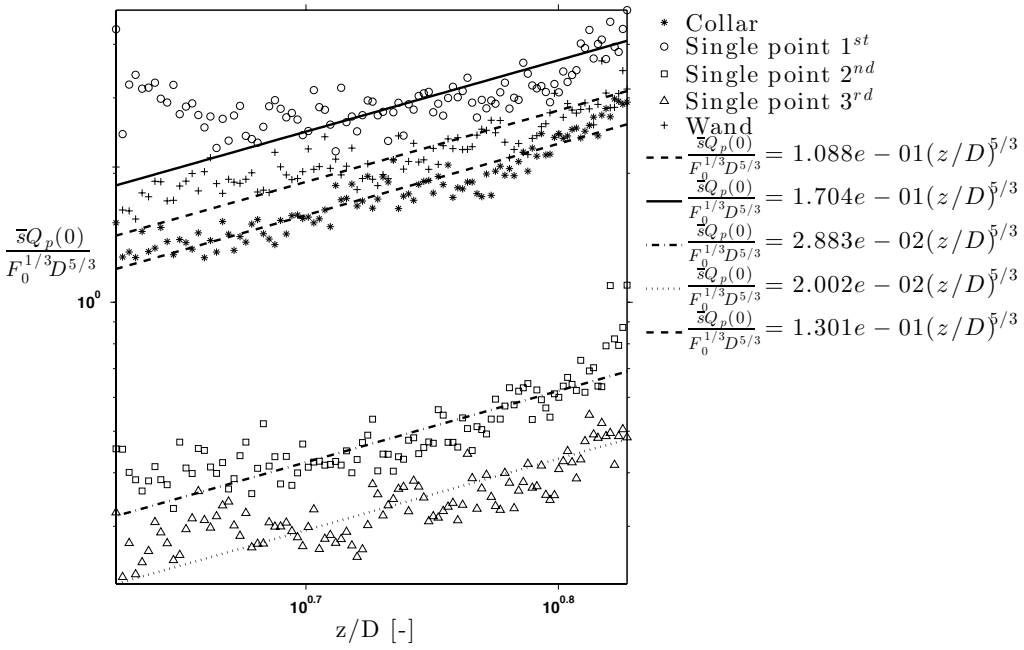

Figure 4-29 Concentration dilution along the plume centerline for 1.0 l/min airflow rate

It can be seen that the single point injector in its second and third position creates a dilution about an order of magnitude smaller than the other types of injectors. To calculate the amount of dilution for each case of the injector type, the concentration values on the centerline of the plume was used. For collar and wand injectors, because of symmetrical property of the concentration field the concentration values on the plume centerline corresponded to the maximum concentration values inside the concentration field. Whereas in the case of the single point injector, the concentration values on the centerline of the plume were not always the maximum concentration values of the created concentration field. That is why the dilution trajectory of the single point injector on the first position shows the same amount of dilution as the collar and wand injectors. The small values of dilution in the centerline agree with the large magnitude fluctuations in the case of single point injector.

4.4 Conclusion

We studied the characteristics of the passive scalar concentration field created by different types of injectors and from various injection points. We measured the instantaneous concentration structure inside a bubble plume with different airflow rates, and by using this data we calculated the time averaged and RMS of fluctuation of the concentration field. Additional information that we derived from the recorded data was the half-width of the plume due to the concentration field and the amount of the centerline dilution for each concentration field. The 3D-PLIF technique enabled us to perform the concentration measurement on different spatial slices of the plume and reconstruct the 3D time averaged concentration field.

Analyzing the data collected and comparing the characteristics of concentration fields of different injectors, we summarized the results from each case below:

1. The collar injector created the most stable concentration field amongst all of injectors. Its concentration field in the y-z plane at each slice was symmetrical around the centerline of the plume and it covers the core of the bubble plume. The concentration fluctuation was limited to the 60% to 70% of the centerline concentration.
2. For the single point injector on its first position, the injected dye solution had strong momentum that in the low airflow rate of the plume the centerline of the concentration was shifted outside of the core of the bubble plume. As it was mentioned before, the centerline of the concentration field and the plume are not aligned in this case, and the maximum values of concentrations were observed at the right edge of the field of view. Using the maximum concentration values in the field of view, the concentration field half-width was about the same as other injector types. On the other hand the magnitude of the concentration fluctuation profile was in the order of the observed maximum concentration values. Also the concentration fluctuation profile is a top-hat shape profile, with its radius three times the half-width of the concentration field. This profile shows the highly intermittent behavior of the concentration field created by the single point injector.
3. For the single point injector on the second position, injection of the tracer dye solution from a distance equal to the momentum length of the effluent helped to keep the concentration field inside the core of the bubble plume. Increasing the airflow rate of the plume broadened the width of the concentration field. Also, the centerline dilution of the generated concentration field was improved as the airflow rate was increased. Compared to the dilution values of other injectors, even this improvement did not change the overall

performance of this injector. Injecting the tracer solution from outside of the plume mixed some part of the tracer dye with the rising fluid in the vicinity of the plume and broadened the width and increased the values of the concentration fluctuation profile compared to the collar injector.

4. The single point injector on the edge of the ZFE has very similar characteristics with the previous case. In this case, the actual distance of the injector and the plume edge was less than the momentum length of the effluent due to width growth of the plume. So the residue of the momentum in the injected tracer solution slightly shifted the concentration field toward the opposite edge of the plume and reduced the efficiency of the created concentration field. Similar to the other cases of dye injection through the single point injector, the single flow of dye effluent did not have a chance to dilute as much as the injection cases of the collar or wand injector.
5. The wand injector created a concentration field with similar behavior as the collar injector. The concentration field was symmetrical around the plume centerline and covered the core of the plume. In contrast to the collar injector, the magnitude of the concentration fluctuation was on the order of the centerline concentration values. Showing the similar trait as the collar injector, the concentration field had an efficient dilution along the plume centerline. The other property of the concentration field created by the wand injector was that increase in the airflow rate of the plume did not have significant effects on the growth rate of the concentration field as the plume rises.

5 SUMMARY AND FUTURE RESEARCH

5.1 Summary

In this dissertation, I focused on the study of the effects of different types of injectors on the characteristics of the passive scalar concentration field inside a bubble plume using the 3D-PLIF technique. The following is a summary of achievements from each chapter of this dissertation:

- Chapter 2: In this chapter, we adapted the 3D-PLIF technique to perform a concentration field measurement on a multi-phase plume. We studied the characteristics of an image recorded from the LIF experiment of a single and multi-phase flow. This gave us the guidelines required to develop new correction processes necessary for obtaining valid data from application of the 3D-PLIF technique in multi-phase flows. One of these new correction methods was removing the bubble signatures and their associated features such as shadows and hot spots from the image database. An image processing technique was developed to generate threshold values required for image segmentation based on pixel characteristics of bubbles. For this purpose, the intensity values of bubble centers were used. Each image was broken down into 64 subsections and the removal process was performed on each subsection individually to achieve the best results possible. The final result of this process was an image free from bubble signatures and their shadows. Finally, to address the light intensification effects of bubbles in the field of view, we used a machine-learning algorithm to measure the bubble distribution probability inside the bubble plume. The amount of light intensification was correlated to the probability of the presence of

bubbles in the field of view. Knowing this probability, we were able to calculate the correlation factor and to correct our image dataset for the effect of light intensification.

- Chapter 3: Using the correction processes developed in chapter one, we used the 3D-PLIF technique to measure the concentration field generated by a collar injector inside a bubble plume with 1.0 [*l/min*] of airflow rate. We verified the correctness of the calculated concentration values from the recorded data by comparing them with the measured concentration values from the experiment tank when uniform dye concentration filled the tank. One of conventional correction methods for the collected data by the LIF technique is removing the lens vignette effects. In previous works, the signature of the vignette effect was extracted from a standard image shot under uniform lighting. In this research we developed a new method to extract the vignette effects from the recorded dataset. In this way, the original vignette signature of the camera chipset is obtained and the final result has perfectly homogeneous intensity values. We extracted the characteristics of the passive concentration field from our experiment and compared it to the available data of a single-phase plume. We were able to verify our method by comparing calculated data from our experiments with well-known characteristics of the concentration field such as its distribution and centerline dilution decay.
- Chapter 4: In this chapter, we studied the physical characteristics of the passive concentration field in a bubble plume created by different types of injectors. Three types of single point, wand, and collar injectors were used for this matter. In the case of the single point injector, we placed it in three different positions to study the

effects of momentum and relative height of injection to the source. We created a bubble plume with three flow rates of 0.5, 1.0, and 1.5 [*l/min*]. In this way, we were able to scale the height of the field of view with different water depth in a hypothetical subsea blow out. The results of this chapter showed that the collar injector was able to create the most stable concentration field with the least amount of fluctuation in the concentration values. In the same context, the single point injector located a momentum length away from the edge of the source has the least stable concentration field. The magnitude of fluctuation in this case was in the same order of centerline concentration, which means there were times during the experiment that no tracer dye was available on the centerline. Another controlling parameter to compare the performance of different injectors is the centerline dilution of the concentration field. Comparing different injectors based on this parameter showed that collar and wand injectors outperformed the single point injector by an order of magnitude. For the single point injector on its first position, strong momentum of the effluent tracer dye shifted the center of the concentration field toward the opposite edge of the plume that the centerline of the concentration field was pushed outside of the field of view. Under this condition, the measured centerline dilution based on maximum concentration values on the field of view showed the same amount of dilution as the collar and wand injectors. The performance of the single point injector on the other two injection points was about the same with slightly better mixing in the second injection point since there was a longer distance between the injection point and the field of view compared to the third injection point. Concentration field spreads the most in the case of single point injector on its second injection point, where the

injector was moved away from the edge of the plume by a momentum length of the dye solution effluent. This is because the injected tracer dye outside of the bubble plume passed through the rising water around it, which in results spread the concentration field wider than the concentration field created by other types of injectors. Under this circumstance, the tracer dye has a better chance to cover a larger area of the plume compared to the collar and wand injectors that inject the tracer dye into the core of the bubble plume.

5.2 Future research

To improve the accuracy and performance of the measurement techniques used in this research and to further investigate the mixing properties in the field of multi-phase plume, we suggest the following list of activities.

- We used intensity threshold to detect and remove bubbles from our image dataset. This method depends on the quantitative properties of image pixels that change from point to point in the image region, and make it challenging to come up with a threshold value that works for the whole image domain. The better approach to this problem is using techniques dealing with the qualitative properties of image constituents. In this way any change in the intensity values of pixels do not compromise the final quality of the process. For this matter, techniques like object recognition are a suitable replacement.
- In this research we had the one field of view over the rising bubble plume. In order to expand the knowledge of mixing properties of multi-phase plume it is a good practice to capture the full length of the plume. Another interesting improvement in the

studying of concentration field measurement is performing the experiments in a stratified environment to investigate the effects of density change on the behavior of the concentration field and mixing properties of the multi-phase plume.

- It is interesting to measure the turbulent mass flux of the bubble plume. For this matter velocity measurement techniques such as Particle Image Velocimetry (PIV) or Bubble Image Velocimetry (BIV) can be combined with the 3D-PLIF technique to have the simultaneous data of velocity and concentration field.

REFERENCES

Allen AA (1990) Contained controlled burning of spilled oil during the Exxon Valdez oil spill. Spill Technology Newsletter 15:1-5

Allen AA, Ferek RJ (1993) Advantages and disadvantages of burning spilled oil International Oil Spill Conference. American Petroleum Institute, pp. 765-772

Andrews HC, Hunt BR (1977) Digital image restoration. Prentice-Hall Signal Processing Series, Englewood Cliffs: Prentice-Hall, 1977 1

Atlas RM (1995) Petroleum biodegradation and oil spill bioremediation. Marine Pollution Bulletin 31:178-182

Banham MR, Katsaggelos AK (1997) Digital image restoration. Signal Processing Magazine, IEEE 14:24-41

Bartlett MS, Littlewort G, Frank M, Lainscsek C, Fasel I, Movellan J (2005) Recognizing facial expression: machine learning and application to spontaneous behavior Computer Vision and Pattern Recognition, 2005 CVPR 2005 IEEE Computer Society Conference on. IEEE, pp. 568-573

Bartlett MS, Littlewort G, Lainscsek C, Fasel I, Movellan J (2004) Machine learning methods for fully automatic recognition of facial expressions and facial actions Systems, Man and Cybernetics, 2004 IEEE International Conference on. IEEE, pp. 592-597

Beier T, Neely S (1992) Feature-based image metamorphosis ACM SIGGRAPH Computer Graphics. ACM, pp. 35-42

Bombardelli F, Buscaglia G, Rehmann C, Rincón L, García M (2007) Modeling and scaling of aeration bubble plumes: a two-phase flow analysis. Journal of Hydraulic Research 45:617-630

Bragg JR, Prince RC, Harner EJ, Atlas RM (1994) Effectiveness of bioremediation for the Exxon Valdez oil spill. Nature 368:413-418

Breiman L (2001) Random forests. Machine learning 45:5-32

Bruun HH (1996) Hot-wire anemometry: principles and signal analysis. Measurement Science and Technology 7:null

Buscaglia GC, Bombardelli FA, García MH (2002) Numerical modeling of large-scale bubble plumes accounting for mass transfer effects. International journal of multiphase flow 28:1763-1785

Canny J (1986) A computational approach to edge detection. Pattern Analysis and Machine Intelligence, IEEE Transactions on:679-698

Carmichael G, Laganière R, Bose P (2010) Global Context Descriptors for SURF and MSER Feature Descriptors Computer and Robot Vision (CRV), 2010 Canadian Conference on. IEEE, pp. 309-316

Cartellier A, Achard J (1991) Local phase detection probes in fluid/fluid two□phase flows. Review of Scientific Instruments 62:279-303

Chanson H (2002) Air-water flow measurements with intrusive, phase-detection probes: Can we improve their interpretation? Journal of Hydraulic Engineering 128:252-255

Cowen E, Chang K-A, Liao Q (2001) A single-camera coupled PTV–LIF technique. Experiments in fluids 31:63-73

Crimaldi J, Koseff J (2001) High-resolution measurements of the spatial and temporal scalar structure of a turbulent plume. Experiments in Fluids 31:90-102

Dalal N, Triggs B (2005) Histograms of oriented gradients for human detection Computer Vision and Pattern Recognition, 2005 CVPR 2005 IEEE Computer Society Conference on. IEEE, pp. 886-893

Daviero G, Roberts P, Maile K (2001) Refractive index matching in large-scale stratified experiments. Experiments in fluids 31:119-126

Davis LS (1975) A survey of edge detection techniques. Computer graphics and image processing 4:248-270

Feng H, Olsen MG, Liu Y, Fox RO, Hill JC (2005) Investigation of turbulent mixing in a confined planar□jet reactor. AIChE journal 51:2649-2664

Ferrier A, Funk D, Roberts P (1993) Application of optical techniques to the study of plumes in stratified fluids. Dynamics of Atmospheres and Oceans 20:155-183

Fingas M (2012) The basics of oil spill cleanup. CRC Press,

Gall J, Razavi N, Van Gool L (2012) An introduction to random forests for multi-class object detection Outdoor and Large-Scale Real-World Scene Analysis. Springer, pp. 243-263

Gall J, Yao A, Razavi N, Van Gool L, Lempitsky V (2011) Hough forests for object detection, tracking, and action recognition. Pattern Analysis and Machine Intelligence, IEEE Transactions on 33:2188-2202

Gandhi V, Roberts PJ, Stoesser T, Wright H, Kim J-H (2011) UV reactor flow visualization and mixing quantification using three-dimensional laser-induced fluorescence. Water research 45:3855-3862

Godec M, Roth PM, Bischof H (2013) Hough-based tracking of non-rigid objects. Computer Vision and Image Understanding 117:1245-1256

Gonzalez RC (2009) Digital image processing. Pearson Education India,

Hearst MA, Dumais ST, Osman E, Platt J, Scholkopf B (1998) Support vector machines. Intelligent Systems and their Applications, IEEE 13:18-28

Herbert P, Gauthier T, Briens C, Bergougnou M (1994) Application of fiber optic reflection probes to the measurement of local particle velocity and concentration in gas—Solid flow. Powder Technology 80:243-252

IBBT E-P (2010) On-line adaption of class-specific codebooks for instance tracking.

Karasso P, Mungal M (1997) PLIF measurements in aqueous flows using the Nd: YAG laser. Experiments in fluids 23:382-387

Katsaggelos AK (2012) Digital image restoration. Springer Publishing Company, Incorporated,

Koochesfahani M, Dimotakis P (1985) Laser-induced fluorescence measurements of mixed fluid concentrationin a liquid plane shear layer. AIAA journal 23:1700-1707

Kovesi P (1999) Image features from phase congruency. Videre: Journal of computer vision research 1:1-26

Kujawinski EB, Kido Soule MC, Valentine DL, Boysen AK, Longnecker K, Redmond MC (2011) Fate of dispersants associated with the Deepwater Horizon oil spill. Environmental science & technology 45:1298-1306

Lee JH-w, Chu V (2012) Turbulent jets and plumes: a Lagrangian approach. Springer Science & Business Media,

Lee JH-w, Chu VH (2003) Turbulent jets and plumes: a Lagrangian approach.

Leibe B, Leonardis A, Schiele B (2008) Robust object detection with interleaved categorization and segmentation. International journal of computer vision 77:259-289

Leitch A, Baines W (1989) Liquid volume flux in a weak bubble plume. Journal of fluid mechanics 205:77-98

Leutenegger S, Chli M, Siegwart RY (2011) BRISK: Binary robust invariant scalable keypoints Computer Vision (ICCV), 2011 IEEE International Conference on. IEEE, pp. 2548-2555

Libby P, WAY J (1970) Hot-wire probes for measuring velocity and concentration in helium-air mixtures. AIAA Journal 8:976-978

Matas J, Chum O, Urban M, Pajdla T (2004) Robust wide-baseline stereo from maximally stable extremal regions. Image and vision computing 22:761-767

McGinnis D, Lorke A, Wüest A, Stöckli A, Little J (2004) Interaction between a bubble plume and the near field in a stratified lake. Water Resources Research 40

Milgram J (1983) Mean flow in round bubble plumes. Journal of Fluid Mechanics 133:345-376

Morris RD (1983) Oil spill recovery means. Google Patents,

Neubeck A, Van Gool L (2006) Efficient non-maximum suppression Pattern Recognition, 2006 ICPR 2006 18th International Conference on. IEEE, pp. 850-855

Papantoniou D, List EJ (1989) Large-scale structure in the far field of byoyant jets. Journal of Fluid Mechanics 209:151-190

Prince RC (1997) Bioremediation of marine oil spills. Trends in Biotechnology 15:158-160

Quinlan JR (1986) Induction of decision trees. Machine learning 1:81-106

Revankar S, Ishii M (1993) Theory and measurement of local interfacial area using a four sensor probe in two-phase flow. International journal of heat and mass transfer 36:2997-3007

Rohlfing T, Brandt R, Menzel R, Maurer CR (2004) Evaluation of atlas selection strategies for atlas-based image segmentation with application to confocal microscopy images of bee brains. NeuroImage 21:1428-1442

Rooney G, Linden P (1996) Similarity considerations for non-Boussinesq plumes in an unstratified environment. Journal of fluid mechanics 318:237-250

Schladow S (1992) Bubble plume dynamics in a stratified medium and the implications for water quality amelioration in lakes. Water Resources Research 28:313-321

Schölkopf B, Smola A (1998) Support Vector Machines. Encyclopedia of Biostatistics

Scholkopft B, Mullert K-R (1999) Fisher discriminant analysis with kernels. Neural networks for signal processing IX 1:1

Seol D-G (2008) Entrainment and mixing properties of multiphase plumes: Experimental studies on turbulence and scalar structure of a bubble plume. Texas A&M University, Ann Arbor, pp. 161

Seol D-G, Bhaumik T, Bergmann C, Socolofsky SA (2007) Particle image velocimetry measurements of the mean flow characteristics in a bubble plume. Journal of engineering mechanics 133:665-676

Socolofsky S, Adams E (2002) Multi-phase plumes in uniform and stratified crossflow. Journal of Hydraulic Research 40:661-672

Socolofsky SA, Adams EE (2005) Role of slip velocity in the behavior of stratified multiphase plumes. Journal of Hydraulic Engineering 131:273-282

Socolofsky SA, Bhaumik T (2008) Dissolution of direct ocean carbon sequestration plumes using an integral model approach. Journal of Hydraulic Engineering 134:1570-1578

Socolofsky SA, Bhaumik T, Seol D-G (2008) Double-plume integral models for near-field mixing in multiphase plumes. Journal of Hydraulic Engineering 134:772-783

Tian X, Roberts PJ (2003) A 3D LIF system for turbulent buoyant jet flows. Experiments in Fluids 35:636-647

Wojek C, Dorkó G, Schulz A, Schiele B (2008) Sliding-windows for rapid object class localization: A parallel technique Pattern Recognition. Springer, pp. 71-81

Wong K, Miller M, Boccabella A (2005) Inclined Boom System With Hydrofoil for Waters With Waves. Proceedings of the 28th Artic and Marine Oilspill Program, Calgary, Canada

Wu Q, Ishii M (1999) Sensitivity study on double-sensor conductivity probe for the measurement of interfacial area concentration in bubbly flow. International Journal of Multiphase Flow 25:155-173

Wüest A, Brooks NH, Imboden DM (1992) Bubble plume modeling for lake restoration. Water Resources Research 28:3235-3250

Yanulevskaya V, Uijlings J, Sebe N (2014) Learning to group objects Computer Vision and Pattern Recognition (CVPR), 2014 IEEE Conference on. IEEE, pp. 3134-3141